Quaternary Science Reviews 305 (2023) 108007

Contents lists available at ScienceDirect

Quaternary Science Reviews

journal homepage: www.elsevier.com/locate/quascirev

Mid-Holocene intensification of Southern Hemisphere westerly winds and implications for regional climate dynamics

Jamie Tamhane [a, b], Zoë A. Thomas [a, b, c, *], Haidee Cadd [b, d], Matthew R.P. Harris [a, e], Chris Turney [f], Christopher E. Marjo [a, b, g], Huixin Wang [g], Rabeya Akter [g], Panayiotis Panaretos [a, b], Amalia Halim [h], Patricia S. Gadd [i], Stefanie Carter [j], Paul Brickle [j, k]

[a] Earth and Sustainability Science Research Centre (ESSRC), School of Biological, Earth and Environmental Sciences, University of New South Wales, Sydney, NSW, 2052, Australia
[b] Chronos ^{14}Carbon-Cycle Facility, Mark Wainwright Analytical Centre, University of New South Wales, NSW, 2052, Australia
[c] School of Geography and Environmental Science, University of Southampton, Southampton, SO17 1BJ, UK
[d] ARC Centre of Excellence for Australian Biodiversity and Heritage, University of Wollongong, Wollongong, 2522 NSW, Australia
[e] School of Geography, Geology and the Environment, Keele University, ST5 5BG, Staffordshire, UK
[f] Division of Research, University of Technology Sydney, Ultimo, NSW, 2007, Australia
[g] Solid State and Elemental Analysis Unit, Mark Wainwright Analytical Centre, University of New South Wales, NSW, 2052, Australia
[h] Tyree X-ray Micro-CT Laboratory, Mark Wainwright Analytical Centre, University of New South Wales, NSW, 2052, Australia
[i] Australian Nuclear Science and Technology Organisation, Lucas Heights, New South Wales, 2234, Australia
[j] South Atlantic Environmental Research Institute (SAERI), Stanley, Falkland Islands
[k] School of Biological Sciences (Zoology), University of Aberdeen, Aberdeen, AB24 2TZ, UK

ARTICLE INFO

Article history:
Received 18 September 2022
Received in revised form
10 February 2023
Accepted 11 February 2023
Available online 1 March 2023

Handling Editor: A. Voelker

Keywords:
Southern hemisphere westerly winds
Dust
Peat
Itrax
Rare earth elements
HYSPLIT
Radiocarbon dating
Amundsen Sea Low
Falkland Islands
Cryptotephra

ABSTRACT

The Southern Hemisphere westerly winds (SWW), a belt of strong zonal winds in the mid-latitudes, play a key role in Southern Hemisphere climate variability. Recent intensification and southwards migration of the SWW is projected to continue due to anthropogenic climate change and despite a recovering Antarctic ozone hole, impacting regional hydroclimate, ocean circulation and carbon cycling. Despite the importance of the SWW, our understanding of their behaviour on centennial to millennial timescales is limited by the inherently short observational record and limited palaeo-archive agreement on the wind belt's Holocene dynamics. Here we utilise dust flux, Itrax core scanning, rare earth element composition and HYSPLIT particle modelling to present a 8700-year (10,500–1700 cal yr BP) reconstruction of local SWW intensity from a Falkland Islands (Islas Malvinas) peat sediment core which, along with other reconstructions, we interpret in a regional South Atlantic and hemispheric context. We find increased dust deposition and variability from ca. 5700 cal yr BP, signalling an intensification and possible southwards shift of the SWW, though Patagonia likely remains the primary distal dust source throughout our record. Additionally, we identify asymmetric behaviour in the SWW belt from 3000 to 1700 cal yr BP over southern South America and the southwest Atlantic. In alignment with these findings, we propose a possible eastwards projection of the Amundsen Sea Low (ASL) into the South Atlantic during this period. Two volcanic eruptions, likely from Mt Burney (ca. 9700 cal yr BP) and Mt Hudson (ca. 4100 cal yr BP), are captured as cryptotephra deposits in the record. Our precisely dated, high-resolution multiproxy record of South Atlantic wind-blown transport provides an important new dataset that accurately constrains SWW Holocene variability over the Falkland Islands.

1. Introduction

The Southern Hemisphere westerly winds (SWW) significantly modulate regional and global climate. Strongest between 50° S and 55° S, the SWW belt expands and contracts around Antarctica on

* Corresponding author. School of Geography and Environmental Science, University of Southampton, Southampton, SO17 1BJ, UK.
E-mail addresses: jamestamhane1@gmail.com (J. Tamhane), z.thomas@soton.ac.uk (Z.A. Thomas).

https://doi.org/10.1016/j.quascirev.2023.108007

seasonal to glacial-interglacial timescales, responding to variations in insolation, regional sea ice, sea surface temperature, and atmospheric temperature gradients (Sime et al., 2013; Varma et al., 2011). In recent decades, the strength of the SWW has intensified and the belt has migrated poleward in response to changing temperature gradients as a consequence of anthropogenic ozone depletion and greenhouse gas emissions, with an associated increase in cloud cover and evaporative heat loss from the ocean (Fogt and Marshall, 2020; Shindell and Schmidt, 2004; Thompson and Solomon, 2002). This trend is likely to continue, with high emissions pathways projecting up to a 1.5° southwards shift and a 10% intensification, compared to current observations (Le Quéré et al., 2007; Perren et al., 2020; Swart and Fyfe, 2012). Although the SWW dominate Southern Hemisphere climate variability, the Amundsen Sea Low (ASL), a quasi-stationary low-pressure system, also plays an important role in modulating regional climate through changes in its location and geopotential height (Clem et al., 2017; Hosking et al., 2013; Thomas et al., 2018).

Future changes in the SWW will likely have significant climatic impacts. For example, earth system modelling suggests shifts in SWW strength and position will impact Southern Hemisphere rainfall patterns (Hill et al., 2009; Jenny et al., 2003; Raut et al., 2014; Risbey et al., 2009), as well as oceanic circulation and nutrient transport (Kohfeld et al., 2013). Future intensification of the SWW is also projected to weaken the Southern Ocean carbon sink, which accounts for ~40% of total global oceanic CO_2 uptake, though there remains large uncertainties about its future behaviour (Frölicher et al., 2015; Landschützer et al., 2015; Le Quéré et al., 2007; Toggweiler et al., 2006). Limited by sparse data points and short term instrumental records, modern SWW studies can only capture interannual to decadal variability (e.g. Landschützer et al., 2015; Le Quéré et al., 2007; Munro et al., 2015; Turney and Fogwill, 2021). Placing modern SWW behaviour and climatic influence in the context of long term (multidecadal to millennial) variation is therefore critical to understanding future SWW changes and climatic impacts.

SWW behaviour is relatively well constrained on seasonal and multidecadal timescales (Garreaud et al., 2013; Marshall, 2003). However, there is little agreement about SWW behaviour on centennial to millennial timescales, where research efforts have focused on the Holocene (Browne et al., 2017; Fletcher and Moreno, 2012; Perren et al., 2020; Turney et al., 2016). Disagreements have been attributed to an overreliance on proxies that indirectly reconstruct past SWW behaviour (via precipitation, sediment geochemistry or changing sub-fossil pollen assemblages), poorly resolved chronologies, and/or confounding continental influences (e.g. the Andes mountain range) (Fletcher and Moreno, 2012; Li et al., 2020; Perren et al., 2020).

To fully understand the SWW's Holocene behaviour, palaeoarchive reconstructions should ideally; be free from continental influences, span the longitudinal range of the SWW belt, have robust chronological frameworks, and be based upon multiple proxies that are sensitive to associated climate and environmental changes (Saunders et al., 2018). Several reconstructions meeting these criteria have been conducted on Sub-Antarctic islands in recent years (Browne et al., 2017; Monteath et al., 2022; Perren et al., 2020; Saunders et al., 2018; Thomas et al., 2018; Turney et al., 2016). However, none of these records from the southwest Atlantic span the entire Holocene. We address this by studying mineral dust deposition in a peat bog archive as it provides a direct measure of windblown transport (Li et al., 2020; Longman et al., 2017; Monteath et al., 2022). The terrestrial source region of dust deposited in our archive is identified through unique geochemical 'fingerprints', manifesting as distinct variabilities in rare earth element (REE) composition (Li et al., 2020; Monteath et al., 2022; Vanneste et al., 2016). Once identified, the dust is used as a proxy for the strength and trajectory of transporting winds (Li et al., 2020; Longman et al., 2017; Marx et al., 2009; Monteath et al., 2022).

This study presents a highly resolved, multi-proxy reconstruction of local SWW behaviour, spanning 10,500-1700 cal yr BP, from a peat bog in the sub-Antarctic southwestern Falkland Islands, which lie in the modern core of the SWW belt (Fig. 1). We compare this record to other reconstructions across the wider Southern Hemisphere to interpret regional and hemispheric climate dynamics.

2. Methods

2.1. Site description

The Falkland Islands are a small archipelago in the South Atlantic, 540 km east of southern South America. Influenced by the surrounding South Atlantic Ocean, the Falkland Islands experience a cool, temperate maritime climate with low seasonal variability and mean annual temperatures of 5.5 °C (Met Office, 2007). The archipelago lies at 52° S, in the core of the modern SWW belt (Fig. 1a,b,c), and experiences high westerly airflow (6-9 ms^{-1}) throughout the year (Upton and Shaw, 2002). In the lee of the Andes mountain range, the Islands experience relatively low precipitation (500–800 mm/year) distributed uniformly throughout the year (Lister and Jones, 2014; Turney et al., 2016). A shift from the climate of the Last Glacial Maximum to the current interglacial period at ca. 16,500 cal yr BP led to the development of extensive blanket peatlands covering large areas (23–45%) of the Falklands (Evans et al., 2017; Wilson et al., 2002). The Falklands' unique combination of SWW dominated airflow, proximity to the South American continent, extensive peatlands, and stable oceanic climate make the archipelago ideal to preserve wind-blown dust from South America (Fig. 1b). Weddell Island is the westernmost major island of the archipelago and is therefore ideally placed to receive South American dust with minimal local input (Fig. 1d). It's geology is part of the Silurian to Devonian Port Stephens Formation, which is mostly composed of sandstone, quartzite and quartz conglomerates (Aldiss and Edwards, 1999). In March 2020, a 2.79 m peat sequence was extracted using a D section corer from an ombrotrophic peat bog at Pond Point, Weddell Island (51.80662° S, 60.87150° W, Fig. 1d). The sod (top 24 cm) was extracted using a shovel to remove the highly fibrous roots and surface vegetation.

2.2. Micro-XRF core scanning

To determine the elemental composition of the sequence, non-destructive X-ray fluorescence (XRF) analysis was performed using an Itrax core scanner (Croudace et al., 2006) at the Mark Wainwright Analytical Centre (MWAC), located at the University of New South Wales (UNSW). Before analysis, the flat surface of each core was smoothed horizontally to minimize measurement error due to an uneven surface (Croudace et al., 2006). Cores were scanned at a 500 μm step size with a 50 s dwell time using a Mo tube set to 30 kV and 55 mA. Itrax data is compositional and collected in counts per second (cps). Low values were eliminated from the top and bottom of each core as they reflect changes in the core surface. Datapoints with summed cps below 40,000 were also removed throughout the core as they likely represent measurement bias due to sedimentological factors (Chagué-Goff et al., 2016; Longman et al., 2019). To analyse compositional data, a principal component analysis (PCA) was applied to the data using R Studio's 'vegan' package (Oksanen et al., 2020).

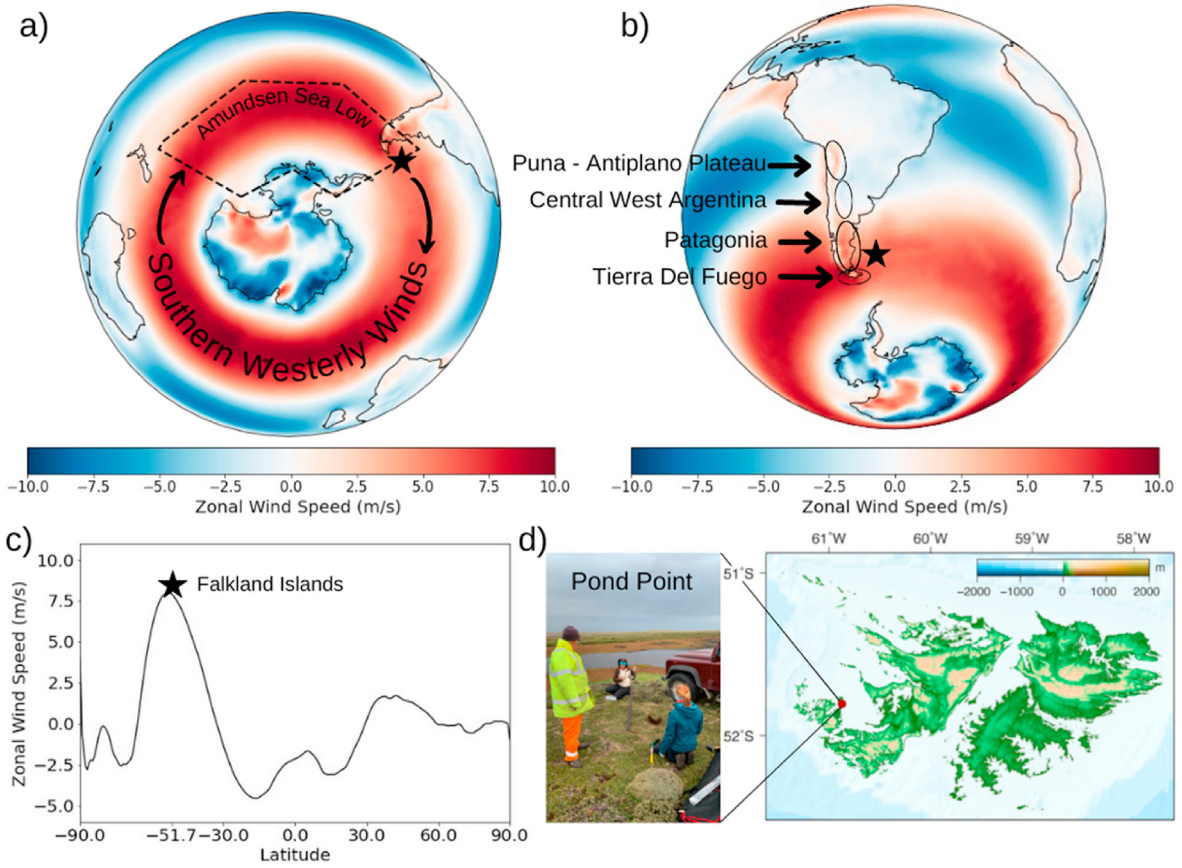

Fig. 1. ***The Southern Hemisphere westerly winds.*** *Average Zonal wind speed 1979-2019 from the ERA-Interim dataset* ***a, b & c*** (Dee et al., 2011). ***a.*** *Location of the Falkland Islands (black star) in the core of the of the SWW belt and in relation to the ASL. The black arrows indicate the direction of the SWW. The black dashed line indicates the modern limits of the ASL defined across the 1979-2001 average* (Fogt et al., 2012; Thomas et al., 2018). ***b.*** *Location of the Falkland Islands (black star) in relation to potential southern South American dust source regions* (Gili et al., 2017). ***c.*** *The Falkland Islands in relation to latitudinal variations in zonal wind speed.* ***d.*** *Location of the core sampling location, Pond Point on Weddell Island, The Falklands.*

2.3. Sedimentological parameters

The cores were sliced into 1 cm sections, and a volumetric subsample was taken and weighed (Heiri et al., 2001). Subsamples were oven-dried at 60 °C for 72 h and re-weighed to determine the dry mass. The bulk density of each sample was calculated by dividing the dry mass by the initial volume of the subsample. Subsamples were placed into pre-weighed crucibles and fired in a muffle furnace at 550 °C for 4 h to remove all organic matter, with the remaining ashed material representing the minerogenic mass. The minerogenic material was then re-ashed at 950 °C to remove carbonate material. The remaining material, referred to as minerogenic dust, was divided by the volume of the initial subsample to determine the amount of dust per cm^3, called the inorganic density.

2.4. Radiocarbon dating & age modelling

A total of 24 bulk sediment peat samples were analysed for radiocarbon dating at the CHRONOS ^{14}Carbon-Cycle Facility, UNSW. Samples were dispersed in Milli-Q water then washed through a 250 μm sieve to remove root and rootlet material, and identify macrofossils (Thomas et al., 2019). Sieved samples were then prepared for dating using an acid-base-acid treatment, following Turney et al. (2021).

A Bayesian age model was constructed in OxCal 4.4 from the radiocarbon age determinations using a 'P_sequence deposition model' (Bronk Ramsey, 2008; Bronk Ramsey and Lee, 2013) with the 'general outlier' analysis detection method (probability = 0.05) (Bronk Ramsey, 2009). The ^{14}C ages were converted into calendar years using the SHCal20 calibration curve (Hogg et al., 2020). The model uses Bayesian statistics, the probability density from radiocarbon calibration, and the stratigraphic order of the sequence to provide a robust age model.

2.5. Rare earth element composition

Rare earth element (REE) composition was determined from 23 samples across a range of inorganic density values. REE's were unlocked from their matrices following a digestion technique developed at MWAC's Solid State & Elemental Analysis Unit that avoids the use of Hydrofluoric Acid. Homogenised minerogenic dust (0.2 g) was weighed into a platinum crucible with a 1:3 ratio of Lithium Borate flux before being fused in a rocking furnace (Claisse TheOx Advanced, Quebec, Canada) at 1050 °C for 2 h, creating a homogenous glass bead. Beads were transferred to a beaker on a hot plate and digested in 70% nitric acid (HNO_3). The resulting solution was analysed for REE composition using a Nexion5000 Multiquad Inductively coupled plasma mass spectrometer (ICP-MS, PerkinElmer, USA) system at UNSW's ICP Laboratory. To determine the validity of results, the PACS-2 (Esquimalt Harbour marine sediment) United States Geological Survey certified reference material was used as a standard (Begum et al., 2007) and blanks were run alongside the samples to calibrate the machine. Good

recoveries for all REE's were observed (~80%).

2.6. Dust and REE flux

Dust flux and REE flux were calculated with equation (2) and equation (3) respectively to quantify the amount of sediment delivered to a core with a varying density and accumulation rate (Li et al., 2020; Marx et al., 2009):

$$Dust\ Flux_i\left(gcm^{-2}yr^{-1}\right) = n.inorganic\ density_i \times bulk\ density_i \times AR_i \times 100. \quad (2)$$

To calculate dust flux, each inorganic density measurement was normalised by 1 gcm^{-3}, producing a unitless, normalised value (given by *n.inorganic density*) for the sample *i*. Bulk density (gcm^{-3}) is the density of the dried sample *i* and the AR is the sediment accumulation rate ($cmyr^{-1}$) at sample *i*, calculated from the age model (Section 2.4).

$$REE\ Flux_i\left(gcm^{-2}yr^{-1}\right) = \sum REE\ /\ UCC_i \times bulk\ density_i \times AR_i \times 100 \quad (3)$$

For REE flux, the concentration of each REE value in sample *i* was normalised by its respective concentration in the upper continental crust (UCC) (Taylor and McLennan, 1995). The values in the sample *i* were then summed to give the total normalised REE concentration for each sample, given by $\sum REE/UCC$.

2.7. Cryptotephra

High inorganic density and elemental Itrax values indicative of inorganic material (e.g., K, Ti, Fe) suggested the likely presence of cryptotephra (microscopic volcanic ash deposits) at two points in the sequence. Fully ashed minerogenic dust from depths 93–94 cm and 174–175 cm (corresponding to peak values) was washed through 90 μm and 25 μm sieves, with the material retained in the 25 μm sieve centrifuged and mounted onto glass slides with Canada balsam (Dugmore, 2008; Pilcher and Hall, 1992). Tephra shards were visually identified using a light microscope at 20x magnification.

2.8. HYSPLIT particle modelling

The Hybrid Single-Particle Lagrangian Integrated Trajectory (HYSPLIT) model (Draxler and Hess, 2015) was used in conjunction with REE composition to provenance the dust found in the peat sequence, and determine similarities between modern and palaeo-air mass circulation. Three-dimensional forward and backward airmass travel histories were reconstructed with input data from the 2.5° NCEP/NCAR reanalysis (Kalnay et al., 1996; available from https://www.ready.noaa.gov/archives.php). To simulate dust-analogous airmass trajectories across a range of SWW behaviours, seasons representing strong, neutral and weak Southern Annular Mode (SAM) Marshall index values (Marshall, 2021, 2003) were selected for HYSPLIT modelling. During the selected seasons, trajectories were modelled for 72 h, and released once per day from the surface of the modelled ground height at each release point. Forward trajectory release sites in southern South America were selected to correspond with the dust source regions sampled in Gili et al. (2017). Back trajectories were released from Pond Point. Further detail can be found in the Supplementary Information (Section 1).

3. Results

3.1. Core composition

The Pond Point sequence covers a total depth of 279 cm. The top 248 cm of the core consists of peat, while lake muds and silty clays sit below. This study focuses on the peat section of the core. See Supplementary Information (Section 2) for more detail on core composition.

3.2. Radiocarbon dates and age model

The age model is presented in Fig. 2. A change in sedimentology was identified between the sod and core sections (between 23 cm and 24 cm, Fig. S2). This change corresponded to a large gap in calibrated ages between 19.5 and 21 cm (−9 cal yr BP) and 34–35 cm (2122 cal yr BP). Therefore, a hiatus was specified in the age-depth model at 24 cm. The cause of the sedimentary hiatus is likely due to historical peat excavation at the sampling location.

Attempts were made to combine the calibrated ages of the seed macrofossils (UNSW-747) and peat at the same depth (UNSW-746) to produce a more robust result, but the two dates were just outside error range. We suggest this difference may be due to peat samples

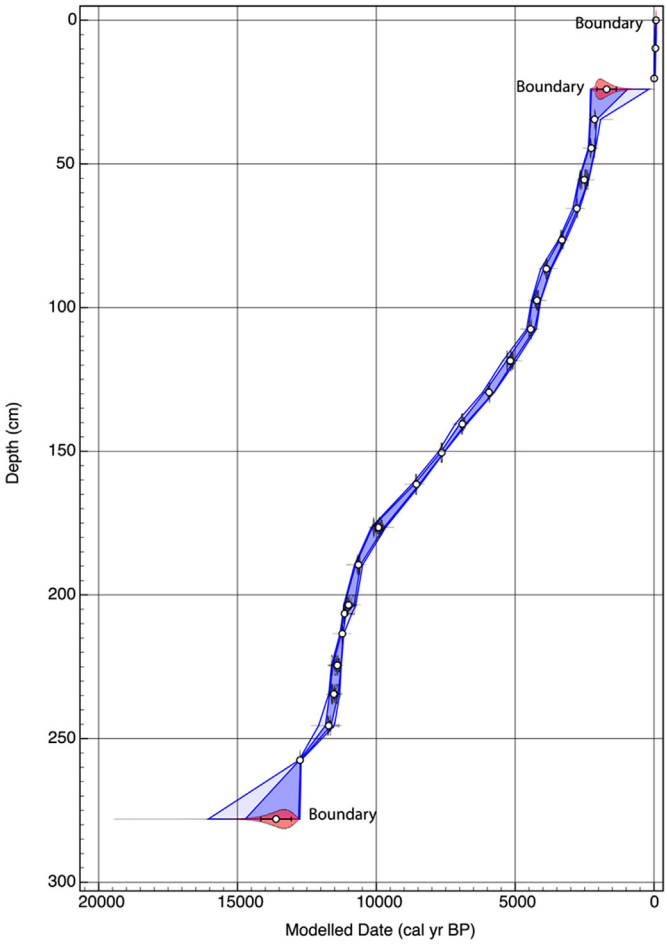

Fig. 2. Age model of the Pond Point sequence constructed from calibrated radiocarbon dates (Table 1). The light and dark blue envelopes show age ranges of 2σ and 1σ respectively. A hiatus (break) was input at 24 cm due to the clear stratigraphic difference between two core sections and the large gap in the calibrated ages (Table 1, Fig. S2). Red shaded areas show input stratigraphic boundaries. The model was run with OxCal 4.4 (Bronk Ramsey, 2017).

Table 1
Radiocarbon and calibrated ages for the Pond Point sequence. Modelled calibrated age range (SHCal20 calibration curve, Hogg et al., 2020) computed in Oxcal 4.4 (Bronk Ramsey, 2017). Calibrated ages are relative to before present (BP) i.e., CE 1950. Errors are ±1σ. Samples UNSW-728 and UNSW-729 are reported as an $F^{14}C$ measurements, and calibrated using the Bomb21_SH1_2 post bomb calibration dataset (Hua et al., 2013).

Laboratory ID	Depth (cm)	F14C*/^{14}C Age (yr BP)	F14C*/^{14}C Age ±1σ (yr)	Modelled mean calibrated age (cal yr BP)	Modelled calibrated age ±1σ (yr)	Material dated
UNSW-728	9–10.5	1.0890*	0.001*	−52	4	Peat
UNSW-729	19.5 −21	1.0333*	0.001*	−9	6	Peat
UNSW-730	34–35	2209	20	2122	71	Peat
UNSW-731	44–45	2227	20	2254	49	Peat
UNSW-732	55–56	2473	20	2502	99	Peat
UNSW-733	65–66	2696	20	2767	38	Peat
UNSW-734	76–77	3151	20	3292	45	Peat
UNSW-735	86–87	3615	20	3848	55	Peat
UNSW-736	97–98	3861	20	4201	62	Peat
UNSW-737	107 −108	3999	20	3999	58	Peat
UNSW-738	118 −119	4564	20	5139	82	Peat
UNSW-739	129 −130	5212	20	5907	46	Peat
UNSW-740	140 −141	6092	20	6861	57	Peat
UNSW-741	150 −151	6852	20	7608	32	Peat
UNSW-742	161 −162	7824	20	8516	42	Peat
UNSW-743	176 −177	8874	20	9881	119	Peat
UNSW-744	189 −190	9464	20	10,616	51	Peat
UNSW-745	203 −204	9613	20	10,988	90	Peat
UNSW-746	206 −207	9808	20	11,121	53	Peat
UNSW-747	206 −207	9665	20	11,121	53	Seeds
UNSW-748	213 −214	9859	20	11,219	19	Peat
UNSW-749	224 −225	10,037	20	11,396	70	Peat
UNSW-750	234 −235	10,050	20	11,525	75	Peat
UNSW-751	245 −246	10,131	20	11,709	63	Peat
UNSW-752	257 −258	10,851	20	12,705	10	Organic Lake Muds

representing an age averaged over a 1 cm section, while the seed represents a single depositional event which may have also been affected by post depositional processes. As both the seed and peat occur at the same depth, they are assigned the same mean calibrated age by the age model.

3.3. Dust flux

Dust flux is characterised by two large peaks in the late Holocene and a clear increase in strength and variability from the late to the early Holocene (Fig. 3a). From 11,800 to 11000 cal yr BP the dust flux is low and moderately variable, with an average of 0.05 $gcm^{-2}yr^{-1}$. The dust flux is at a minimum from 11,000 to 5700 cal yr BP with average values of 0.02 $gcm^{-2}yr^{-1}$, except for a peak at ca. 9700 cal yr BP, representing a cryptotephra deposit (Section 3.4). From 5700 to 1700 cal yr BP, the dust flux becomes higher and more variable with peaks at 4800–2500, 3700–3400 and 2300-1700 cal yr BP. The largest peak on the record at ca. 4100 cal yr BP indicates another cryptotephra deposit. Modern (−70 to 0 cal yr BP) values are highly variable, ranging from 0.04 to 1.44 $gcm^{-2}yr^{-1}$ (Fig. S2) and are likely to be influenced by the unhumified nature of the sod.

3.4. Cryptotephra deposits

High concentrations of tephra shards were identified in the sequence at 174–175 cm and 93–94 cm, confirming the spikes of inorganic material at ca. 9700 and 4100 cal yr BP are cryptotephra deposits (Fig. 3, S2, S3). The cryptotephra deposit at ca. 9700 cal yr BP coincides with the eruption of Mt Burney (MB1), which has previously been detected in the Falklands (Monteath et al., 2019). Glass shard morphologies (Smith et al., 2019) for this deposit are cuspate, fluted and bubble-walled. Some shards are moderately to densely vesicular (Fig. S3b). The cryptotephra deposit at ca. 4100 cal yr BP roughly coincides with the eruption of Mt Hudson (H2), an eruption previously detected in Falklands peat records (Panaretos et al., 2021). Glass shard morphologies for this deposit (Smith et al., 2019) are predominantly cuspate and fluted (Fig. S3a). The origin of these deposits will be confirmed through further geochemical analysis and chemical fingerprinting of glass shards, allowing for chemical correlations to known eruptions (Panaretos et al. in prep).

3.5. Itrax elemental composition

Itrax core scanning detected 37 elements. Elements P, Cl, Cs and Pb were removed from further analysis due to high numbers of measurements with 0 cps. Itrax values before 11,700 cal yr BP are not interpreted due to the influence of lake muds (Fig. 3b and c).

The ratio of Si/Fe was used as a proxy for grain size. Fe is associated with fine particles and Si with coarse-grained particles (Cuven et al., 2010). Higher ratio values are therefore associated with coarser grains. 11,600-10100 cal yr BP has the lowest Si/Fe ratio, indicating finer grained material. The ratio increases and is more variable from 10,100 to 4900 cal yr BP. From 4900 cal yr BP there is a shift to larger proportions of coarse grains and moderate variability for the rest of the record. 2400-1700 cal yr BP has the highest proportion of coarse grains, peaking at 2100 cal yr BP.

The principal components analysis was applied to the peat section of the Pond Point sequence (Fig. S2). The first axis (PC1) of the PCA biplot (Fig. S4) explains 23% of the variance and describes the strong relationship between the minerogenic elements of K, Si and Ti. These elements have a more moderate relationship with Fe. PCA Axis 1 is highly influenced by the Mt Burney cryptotephra deposit at ca. 9700 cal yr BP, a peak at ca. 5100 cal yr BP and the Mt Hudson cryptotephra deposit at ca. 4100 cal yr BP. Despite being able to identify the two cryptotephra deposits, PCA Axis 1 is not solely representative of tephra deposition. Instead, it is likely detecting the minerogenic elements (e.g., Si, Ti, K) contained within the tephra shards that are also present in the minerogenic material and lake muds. From 11,700 to 10000 cal yr BP values are at a minimum, though they remain variable. Values slightly increase and become less variable from 10,000 to 1700 cal yr BP, remaining reasonably consistent (Fig. 3c). See Supplementary Information (Section 6) for detail on PCA Axis 2.

3.6. Rare earth element composition

Individual Rare Earth Element (REE) normalised concentrations range between 0.3 and 1.5, while concentrations within samples typically stay within a range of less than 0.83 (Fig. 4a). Samples at

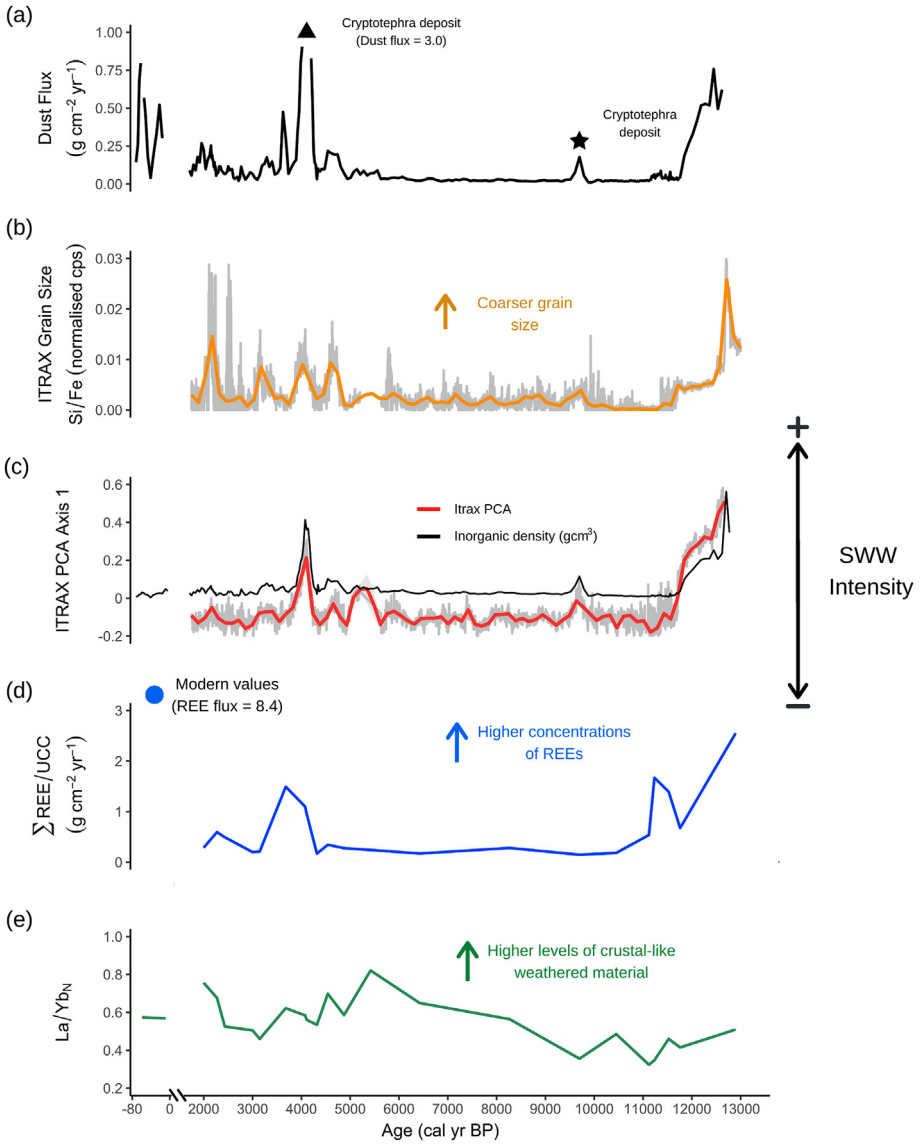

Fig. 3. Proxies for local SWW intensity. Itrax data was loess smoothed with a span of 0.01. Gap in Itrax data from 5630 to 5200 cal yr BP due to instrumental error. a. Dust flux calculated from equation (2). Y axis has been truncated at 1 gcm^{-2}yr^{-1} to reduce the influence of a cryptotephra peak. Cryptotephra deposits are marked at ca. 9700 cal yr BP (black star) and ca. 4100 cal yr BP (black triangle). b. Si/Fe ratio of Itrax data, representing grain size. A higher value indicates a larger proportion of coarse grains. c. Axis 1 of the PCA analysis conducted on the Itrax data (red line). Inorganic density (black line) is plotted to demonstrate the strong similarities between the two ($R = 0.92$, $p < 0.0001$). d. REE flux calculated from equation (3). Y axis has been truncated for better visibility of Holocene variations otherwise masked by large modern values. e. La/Yb$_N$ ratio from UCC normalised REE composition data. A higher value indicates higher inputs of weathered material from igneous rocks (Monteath et al., 2022).

11,760–11120 and 8270 cal yr BP have higher individual elemental concentrations that range from 0.79 to 6 and higher variation within samples, with differences in concentrations as high as 3.95. The sample at 2000 cal yr BP has much lower individual concentrations (0.28–0.4) and range (0.12) than all other samples. We therefore infer the samples at 11,760–11120, 8270 and 2000 cal yr BP are distinctly different from the rest of the samples. The similar elemental concentrations and patterns between the rest of the samples illustrate the high relatedness of this sample group.

Dust provenance was examined by comparing the Eu/Eu* and La/Yb$_N$ relationships (REE indicators of distinct geochemical composition) of minerogenic dust in the Pond Point sequence to a southern South American reference dataset (Gili et al., 2017). Samples at 12,900–11120, 9700, 4870, 4320–4080, 3150, 2430 and −10 cal yr BP lie outside of all southern South American reference spaces (Fig. 4b). Given the record consists of lake muds before 11,800 cal yr BP (Fig. S2), it is likely that the sample at 12,900 cal yr BP is confounded by local minerogenic material. While the samples 11,760-11120 cal yr BP are within the peat section of the record, they have distinctly different REE concentrations from the rest of the peat samples (Fig. 4a). Given the proximity of Pond Point to southern South American dust source regions and persistent westerly airflow over the Falklands (Fig. 1, Section 2.1), it is highly unlikely that these samples represent dust from other Southern Hemisphere source regions, such as Australia or southern Africa. We therefore infer that these samples have been affected by local depositional processes (such as local material washed into the lake basin) that mask the presence of southern South American dust. The samples at 9700 and 4320-4080 cal yr BP lie within the peaks of the Mt Burney and Mt Hudson cryptotephra deposits, with high concentrations of tephra shards likely confounding the geochemical analysis. While the samples at 4870 and 3150 yr BP do

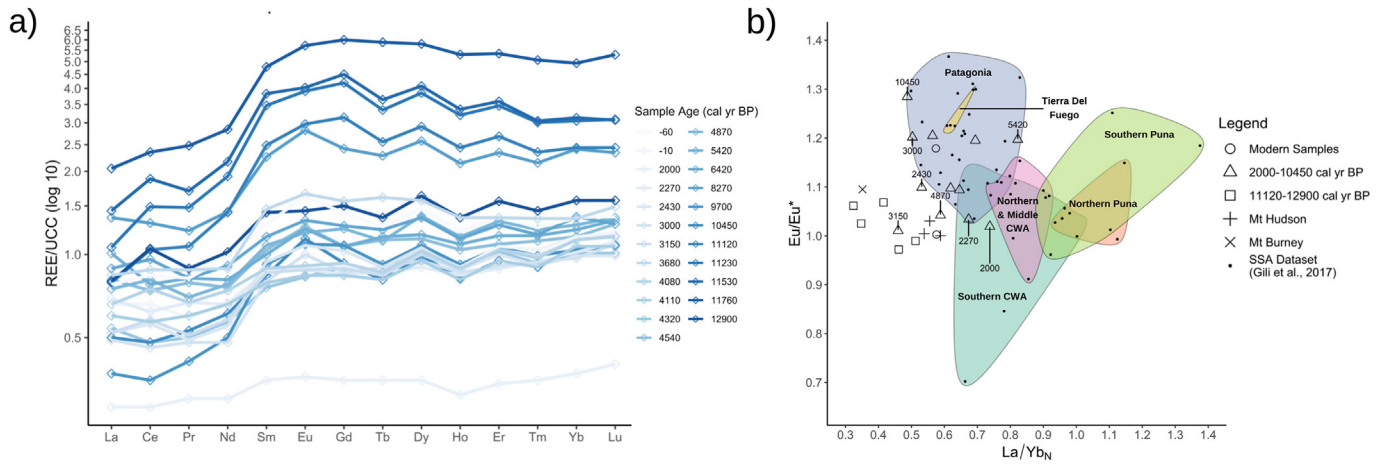

Fig. 4. All values have been normalised to their respective concentrations in the upper continental crust (UCC) (Taylor and McLennan, 1995). a. REE concentrations. Samples are coloured by age, with darker blues indicating older samples. b. Pond Point Eu/Eu* and La/Yb_N values compared to southern South American reference values from dust source regions (Gili et al., 2017). Eu/Eu* was calculated as $\frac{Eu_N}{\sqrt{Gd_N \times Sm_N}}$ (Taylor and McLennan, 1995). Central West Argentina is shortened to CWA, and the Southern Altiplano region (La/Yb_N values > 1.2) has been excluded for data visualisation. Ellipses were drawn with data from Gili et al. (2017). Samples from the modern period (−10 and −60 cal yr BP) are denoted with a circle. Samples spanning the period of 10,450–2000 cal yr BP are denoted with a triangle, outliers and a range of samples from this period are labelled with the sample's age in cal yr BP. Samples older than 11,120 cal yr BP are denoted with a square. Samples within the Mt Burney (9700 cal yr BP) and Mt Hudson (4320-4080 cal yr BP) cryptotephra peaks are also identified with a cross and a plus respectively.

not lie within obvious cryptotephra deposits, 4870 ($1\sigma = \pm 73$) cal yr BP aligns with the largest-volume Holocene eruption of Chaitén (Cha2), dated at 4950 ± 100 cal yr BP (Watt et al., 2013). Additionally, 4870 cal yr BP has been identified as a likely age for cryptotephra deposits in other Falkland Islands records (P. Panaretos, personal communication). The sample at 3150 ($1\sigma = \pm 42$) cal yr BP aligns roughly with the Aguilera 1 (A1) eruption, dated at 3000 ± 100 cal yr BP (Stern, 2008) and 2978 +91/-104 cal yr BP (Klaes et al., 2022), which has an easterly dispersion axis (Stern, 2008). It is therefore possible that these samples have been confounded by the presence of cryptotephra deposits, though they have not been examined for tephra shards. The sample at 2430 cal yr BP, while not falling within the Patagonia reference space, is assumed to be similar enough when accounting for possible variation in the Eu/Eu* and La/Yb_N relationships that is not captured in the reference dataset. The two samples from the modern period are variable, with the sample at −10 cal yr BP lying outside of all reference spaces, but the sample at −60 cal yr BP lying within the Patagonian reference space. It is possible that the sample at −10 cal yr BP has been affected by anthropogenic activities or local depositional processes, however, given the small number of datapoints, we cannot confidently provenance dust with REE concentrations in the modern period. From the 11 samples uninfluenced by cryptotephra deposits in the period 10,450-2000 cal yr BP, eight fall clearly within the Patagonian reference space, while the sample at 2000 cal yr BP falls within southern CWA. Therefore, the results of this analysis suggest that dust deposited between 10,450 and 2000 cal yr BP originated primarily from Patagonia, with a possible minor southern central west Argentina component at ca. 2000 cal yr BP.

REE flux is characterised by large peaks in the early and late Holocene with relatively consistent values throughout the mid Holocene. From 11,800 to 11,000 cal yr BP REE flux peaks, before declining till 10,500 cal yr BP (Fig. 3d). REE flux is at a minimum from 10,500 to 4500 cal yr BP, with an average value of 0.23 $gcm^{-2}yr^{-1}$. From 4500 to 2000 cal yr BP REE flux increases, peaking at ca. 3700 cal yr BP. Similar to dust flux, modern (−10 to −60 cal yr BP) values are high, peaking at 8.44 $gcm^{-2}yr^{-1}$ (Fig. 3d) and are also likely influenced by the unhumified nature of the surface sediments.

La/Yb_N is characterised by an increase in the late Holocene compared to the early Holocene (Fig. 3e). From 11,800 to 9700 cal yr BP the ratio is at a minimum, with a mean value of 0.76. From 9700 cal yr BP values steadily increase, peaking at 5400 cal yr BP. From 5400 cal yr BP the ratio declines till 3100 cal yr BP, though remains higher than the early Holocene, before increasing till 2000 cal yr BP. Modern values are consistently moderate compared to the late Holocene, with an average of 0.57.

3.7. HYSPLIT trajectory modelling

Though our use of HYSPLIT is restricted to modern meteorological data, previous observational and modelling studies have demonstrated that strong similarities between modern and palaeo-wind conditions exist, allowing for parallels to be drawn between modern and palaeo-air mass circulation (De Vleeschouwer et al., 2014; Fagel et al., 2008; Haug et al., 2001; Kilian and Lamy, 2012; Markgraf et al., 2000).

Despite our release of trajectories spanning time periods encompassing the full range of SWW belt variations across with the late 20th and early 21st centuries, a clear boundary at ~35° S is present between the southern South American dust source regions. Forward trajectories released from the sites north of 35° S do not reach the Falklands in any of the modelled meteorological scenarios, while back trajectories show no contributions from areas north of 35° S. In comparison, sites south of 35° S consistently have forward trajectories that reach the Falklands, with high concentrations of back trajectories across these sites (Fig. S5).

4. Discussion

4.1. Minerogenic deposition

Previous studies have recorded post-depositional mobilisation of elements in peat bogs via groundwater leaching or organic processes such as decomposition and redox cycling (Longman et al., 2017; Novak et al., 2011; Rothwell et al., 2010; Yang et al., 2021). However, Ti and Si have been shown to be highly immobile and conservative elements in peat bogs (Bozau et al., 2021; Novak et al., 2011), and have a strong positive relationship to the mobile

elements of K and Fe in the Pond Point sequence (Fig. S4). This indicates that the distribution of elements representing minerogenic inputs in the Pond Point sequence is largely unaffected by post-depositional mobilisation processes. Combined with a high organic matter (average = 79%) and low bulk density (average = 0.17 gcm^{-3}), the Pond Point peat record can be defined as ombrotrophic, meaning that it receives all inputs (e.g. minerogenic, nutrients, moisture) via atmospheric loading (Longman et al., 2017). This record can therefore provide a robust record of past atmospheric minerogenic deposition.

The strong positive relationship between elements indicating minerogenic inputs via atmospheric loading with PCA Axis 1 (Fig. S4) demonstrates its effectiveness as a proxy for minerogenic deposition. The high correlation between PCA Axis 1 and inorganic density ($R = 0.92$, $p < 0.0001$, Fig. 3c) validates the dust flux as a proxy for minerogenic deposition to a core with a varying density and accumulation rate. Variations in ratios of elements associated with coarse (e.g. Si, Zr) and fine (K, Fe, Ti) grained particles has been proven to be an effective qualitative proxy for grain size in peat records (Chawchai et al., 2016). While Chawchai et al. (2016) uses Si/Ti as an indicator of minerogenic grain size variations, Si/Fe was selected in this study as Ti and K have many 0 cps values in the younger sections of the sequence, indicating high noise levels. REE flux has been proven to be a valid method of examining changes in minerogenic deposition (Hooper et al., 2020; Li et al., 2020). The relationship between REE flux and dust flux (Fig. 3a, d), evidenced by concurrent peaks in intensity, further lends support to the validity of our use of dust flux. The ratio of La/Yb_N was used as another proxy for minerogenic deposition. While Pond Point is located on a quartz sandstone (a sedimentary rock) outcrop of the Port Stephens formation (Aldiss and Edwards, 1999), silicic igneous rocks make up large portions of the Andes mountain range (Gaiero et al., 2004; Monteath et al., 2022). As igneous rocks are associated with higher La/Yb_N values than sedimentary rocks, in the context of this study, we interpret high values of La/Yb_N as indicating higher levels of minerogenic deposition from Patagonia (Monteath et al., 2022). The close relationships observed in the variations between the minerogenic deposition proxies (Fig. 3) provides confidence in the use of these proxies for reconstructing atmospheric dust fluxes.

4.2. Dust provenance

Through distinct REE compositions and HYSPLIT modelling, the source of minerogenic dust deposited into the Pond Point sequence can be identified. Convergence of forward and back HYSPLIT trajectories across a range of meteorological scenarios highlights the consistent contribution of particles from southern Patagonia and Tierra del Fuego to Pond Point (Fig. 5). While no REE reference dataset exists for the Falkland Islands, its geology is closely related to southern Africa (Monteath et al., 2022; Stone, 2015), which has distinctly different REE compositions to southern South America (Li et al., 2020). Our REE analysis (Section 3.6, Fig. 4b), indicates it is highly likely that the vast majority of minerogenic dust deposited into the sequence from 10,500 to 1700 cal yr BP originates from Patagonia, while the outlying REE samples are influenced by tephra or local minerogenic input. Outlying samples from 11,760 to 11,120 cal yr BP occur concurrently with the highest variation in PCA Axis 2 (Fig. S6). While modern meteorological data was used to represent Holocene airmass circulation in HYSPLIT modelling, and REE samples suitable for dust provenancing have a coarse temporal resolution in our record, these analyses both highlight Patagonia as the primary source of dust in our record. This result aligns with findings in Monteath et al. (2022), a similar wind-blown dust record from the Falkland Islands. We therefore infer that southern South America and specifically Patagonia is the source of the vast

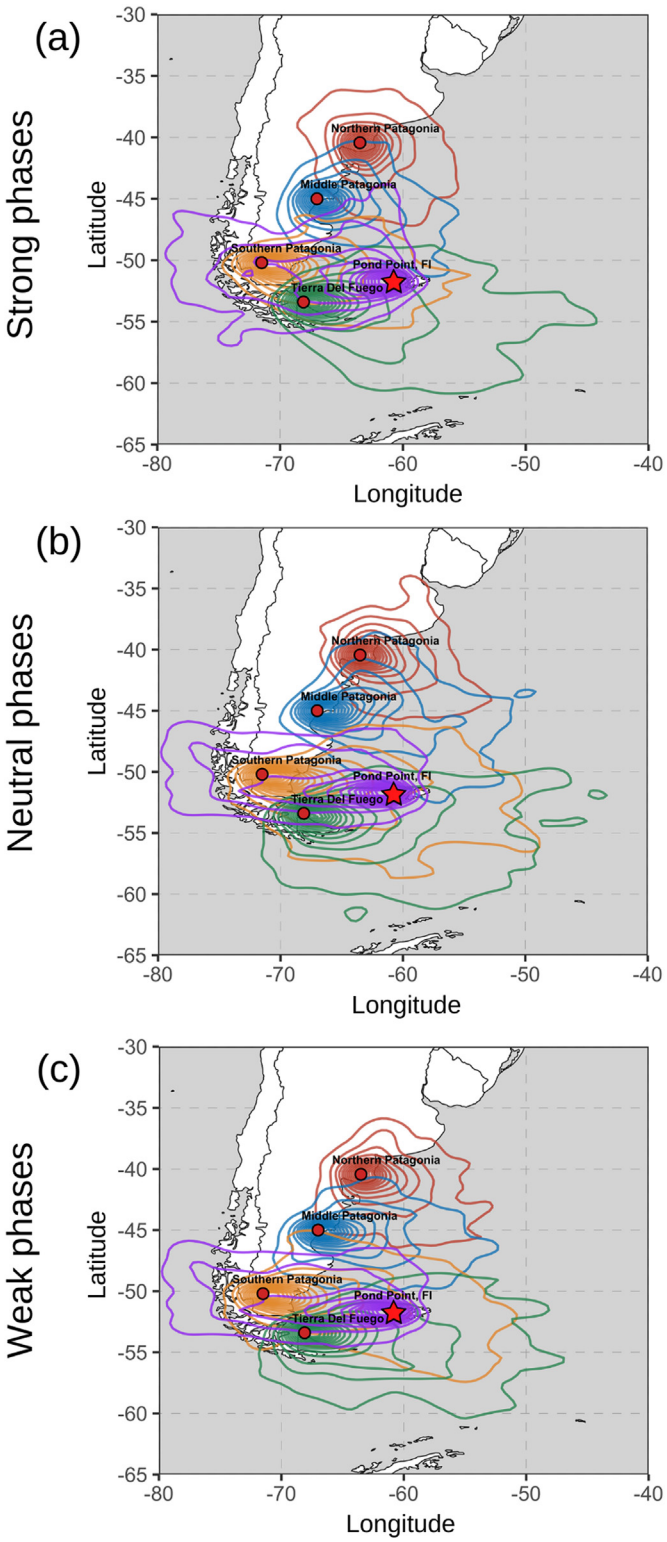

Fig. 5. Densities of 72 h HYSPLIT forward trajectories from southern South American sites (circles) and back trajectories from Pond Point (star). Each plot shows the combined seasonal trajectories for strong, neutral and weak SAM phases (a, b, c respectively) (table S1). Each colour represents the trajectories released from a single site. While trajectories were calculated in 12 different scenarios, there was no change in the interactions between sites north and south of 35° S. Seasonal trajectories were therefore combined for easy visualisation.

majority of minerogenic material in the record from 10,500 to 1700 cal yr BP.

4.3. SWW proxy interpretation

Atmospheric circulation in the Falklands is dominated by the SWW (Fig. 1). By identifying southern South America as the primary source of minerogenic dust from 10,500 to 1700 cal yr BP, changes in these proxy relationships can be interpreted as relative changes in SWW intensity at Pond Point during this period. This study uses multiple independent proxies to measure dust deposition, providing reliable evidence of past local SWW behaviour. Given that stronger SWW mobilise and transport more dust, it is inferred that periods of elevated (lower) dust flux indicates stronger (weaker) SWW intensity (Marx et al., 2009). The relative changes in elements indicative of minerogenic deposition (represented by PCA Axis 1, REE flux and La/Yb_N) can be used as separate proxies for changes in SWW intensity (Lewis et al., 2020; Li et al., 2020; Monteath et al., 2022; Saunders et al., 2018). With the same relationship as dust flux, higher (lower) PCA Axis 1, REE flux and La/Yb_N values indicate periods of stronger (weaker) SWW intensity. Given that stronger SWW mobilise and transport coarser grains (Stuut et al., 2002; Turney et al., 2017), a period of higher (lower) Si/Fe ratios represents a higher (lower) proportion of coarse-grained particles mobilised and deposited into the core. Therefore higher (lower) Si/Fe ratios represent stronger (weaker) SWW intensity.

Changes in distal dust source regions can act as a proxy for the latitudinal position of the SWW belt (Gili et al., 2017). Source areas of distal dust deposited into the sequence are identifiable through distinct variabilities of REE composition and HYSPLIT modelling. These techniques demonstrate Patagonia is the primary dust contributor to the Falklands over the Holocene (Fig. 4b), with possible minor contributions from southern central west Argentina. However, HYSPLIT also indicates contributions from Tierra del Fuego, likely masked in the REE signature by the dominance of Patagonian dust (Fig. 5). Patagonia spans a large latitudinal range (from 38° S to 51° S) (Fig. 1b), and REE and isotopic signatures alone cannot divide Patagonia into smaller sub-regions (Gili et al., 2017; Li et al., 2020), limiting tracking of SWW latitudinal movements. While the REE sample at 2000 cal yr BP appears to originate from southern Central West Argentina, we cannot confidently interpret an extended latitudinal shift in the SWW from one datapoint. Our results therefore indicate no extended shifts of the SWW outside the latitudinal range of Patagonia during the Holocene. However, it is likely that shifts inside this range occurred, reflected by changes in the dust flux, grain size, PCA Axis 1 and other reconstructions (Gray et al., 2021, in press; Monteath et al., 2022; Voigt et al., 2015). The coarse resolution of the REE analysis does not capture decadal or centennial-scale changes in the position of the SWW, masking potential migrations. Further sampling of Patagonian dust or novel provenancing methodologies would be needed to track latitudinal variations of the SWW on finer temporal and spatial scales.

REE signatures cannot accurately constrain the latitudinal movement of the SWW belt over the Holocene. However, parallels can be drawn between modern and palaeo-air mass-circulation by selecting meteorological scenarios (i.e., SAM phases) where trajectories skew towards maximum input from Patagonian sites and minimal input from Tierra del Fuego.

The scenarios best meeting this criterion are Neutral Summer (2003) and Weak Spring (2002) (Fig. S7, Table S1). No clear relationship is evident however, between SWW position and contributions of particle trajectories to the Falklands from different release regions. See Supplementary Information (Section 7) for further detail.

4.4. Addressing proxy assumptions

South American dust emissions vary on seasonal, interannual and centennial to millennial timescales in response to changes in vegetation cover, precipitation, anthropogenic land use and SWW latitudinal position (Gassó and Torres, 2019; Huber and Markgraf, 2003; Jara et al., 2019; Mercer and Ager, 1983). Changes in each of these variables could impact minerogenic deposition into the Pond Point sequence, confounding interpretations of SWW behaviour. Postglacial climates of southern South America suggest a general increase in precipitation since the Pleistocene-Holocene transition. Increases in precipitation and temperature since ca. 12,500 cal yr BP resulted in the expansion of open Nothofagus forests on the western side of the Andean Mountain range and the development of shrub or grass steppe in eastern regions (Echeverría et al., 2022; Mancini, 2009; Tonello et al., 2009). Wet conditions and expansion of closed Nothofagus forests dominated the early to mid-Holocene in most regions of southern South America. This period coincides with an increase in Andean glacial advance from 6900 to 4200 cal yr BP, suggestive of cold and moist conditions (Kaplan et al., 2016). The late Holocene from 4200 cal yr BP-present is characterised by the most variable climates of the Holocene, however many records from southern South America indicate that from ca 3600 cal yr BP vegetation in the region was stable (Álvarez-Barra et al., 2020; De Porras et al., 2008; Pendall et al., 2001). Increased or stable vegetation cover decreases dust availability (Mancini, 2009), which should have reduced dust emissions (Marx et al., 2018). However, a period of weakened minerogenic deposition is not seen in the Pond Point sequence during the late Holocene (Fig. 5). This may suggest that southern South American vegetation cover is not significantly impacting the dust record at Pond Point. However, the heterogeneity of climates and vegetation across southern South America and limited number of records available from the region since the late Pleistocene indicate additional complexity that may influence the dust availability to our record. While interannual and interdecadal variabilities are not captured in the peat record due to its temporal resolution, seasonal variations may influence interpretations of SWW position. Patagonian dust emissions peak in austral summer, when the SWW belt migrates south (Bory et al., 2010; Gassó and Torres, 2019). Therefore, the majority of the dust deposited in the core was likely mobilised in summer, providing a summer-dominated picture of SWW behaviour.

4.5. Holocene dynamics of the SWW

Dust flux was compared with other paleo-atmospheric and oceanographic proxies to interpret local SWW behaviour in the context of hemispheric-wide changes (Fig. 6).

4.5.1. Late glacial - early Holocene: 13,600-10500 cal yr BP

As demonstrated in the REE analysis (Section 3.6), local material appears to dominate minerogenic input in the record till 10,500 cal yr BP. We therefore do not interpret our record as representative of SWW behaviour during this period.

4.5.2. Early Holocene: 10,500-6000 cal yr BP

Dust flux and the other intensity proxies are weak in the early Holocene (Fig. 3), indicating weak local SWW intensity, an interpretation aligning with other Falklands reconstructions (Fig. 6c) (Groff et al., 2020; Monteath et al., 2022). While the Mt Burney

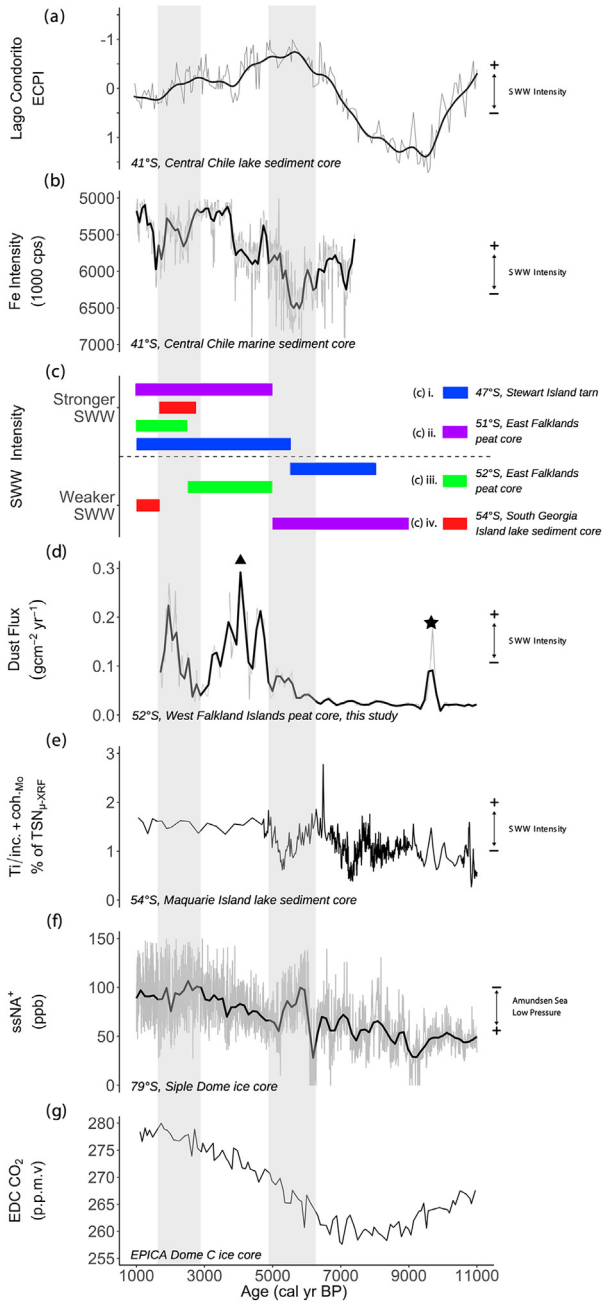

Fig. 6. Comparison of the Pond Point Sequence to other SWW and atmospheric reconstructions. Grey bars mark significant time periods. a. Eucryphia + Caldcluvia/podocarps index (ECPI) from a lake sediment core in central Chile (Moreno, 2004; Moreno et al., 2010). b. Fe Intensity from marine sediment core GeoB3313-1 in central Chile (Lamy et al., 2001). c. Periods of strong and weak SWW from records where SWW behaviour was interpreted by combing multiple proxies. i. Blue.— Tarn from Stewart Island, southern New Zealand (Turney et al., 2017). ii. Purple — Peat core from Surf Bay, eastern Falkland Islands (Groff et al., 2020). iii. Green - Peat core from Canopus Hill, eastern Falkland Islands (Thomas et al., 2018). iv. Red — Lake sediment core from Fan Lake, South Georgia Island (Strother et al., 2015). d. Loess smoothed (span = 0.05) dust flux from this study, with Mt Burney (black star) and Mt Hudson (black triangle) tephra deposits marked. e. Normalised Ti data, obtained by Itrax core scanning from a lake sediment core on Macquarie Island (Saunders et al., 2018). f. $ssNa^+$ aerosol flux, a proxy for ASL pressure, from a Siple Dome Ice core, West Antarctica (Mayewski et al., 2013). g. Atmospheric CO_2 concentrations from EPICA (European Project for Ice Coring in Antarctica) Dome C (EDC), East Antarctica (Monnin et al., 2004).

cryptotephra deposit manifests as a spike in all proxies at ca. 9700 cal yr BP, this does not indicate a change in SWW behaviour (Fig. 3). Regionally, reconstructions from all sectors of the southern mid-latitudes experienced relatively weak SWW intensity during this period, consistent with this study (Fig. 6b,c,d,e) (Groff et al., 2020; Kaplan et al., 2020; Monteath et al., 2022; Moreno et al., 2021, 2010; Saunders et al., 2018; Turney et al., 2017). However, between these records, there are differing interpretations of SWW position. Reconstructions disagree on whether the SWW were displaced north (Voigt et al., 2015) or south (Gray et al., 2021; Kaplan et al., 2020; Monteath et al., 2022) of their modern position, or whether the weak SWW intensity is due to reduced baroclinity of the atmosphere (Moreno et al., 2021). While our record cannot determine which of these interpretations is correct, it lends further evidence to the notion of weak intensity in the core of the SWW belt during the early Holocene.

4.5.3. Mid Holocene: 6000-5000 cal yr BP

At ca. 5700 cal yr BP, dust flux triples in strength, and grain size, PCA Axis 1 and La/Yb_N values increase, indicating an intensification of the SWW over the Falklands (Fig. 3). This change is consistent with other reconstructions, which see an increase of SWW intensity in records from the northern (Fig. 6b and c) and core regions of the SWW (Fig. 6c,d,e) (Groff et al., 2020; Lamy et al., 2001; Li et al., 2020; Mayewski et al., 2013; Moreno et al., 2010; Saunders et al., 2018; Turney et al., 2017). The strong agreement between records across the longitudinal extent of the SWW, utilising ecological (Groff et al., 2020; Moreno et al., 2010; Strother et al., 2015), oceanic (Lamy et al., 2001) and atmospheric proxies (Saunders et al., 2018; Thomas et al., 2018; Turney et al., 2017), lends confidence to interpreting these increases as an intensification across the northern and core regions of the SWW belt. From similar behaviour observed in modern records and other SWW reconstructions, a possible mechanism for this intensification is a latitudinal migration of the SWW belt (Fogt and Marshall, 2020; Li et al., 2020; Monteath et al., 2022; Perren et al., 2020). However, reconstructions from the regions south of the core SWW belt do not record an intensification in this period (Kaplan et al., 2020; Shevenell et al., 2011). This is possibly due to a mid-Holocene migration or latitudinal contraction of the southern extent of the SWW belt between Chile and the West Antarctic Peninsula (Etourneau et al., 2013), or confounding local Antarctic climatic influences.

4.5.4. Late Holocene: 5000-1700 cal yr BP

Dust flux, PCA Axis 1 and grain size further increase in the late Holocene (Fig. 3), indicating higher SWW intensities over Pond Point than the mid-Holocene. From 4400 to 3400 cal yr BP, the Mt Hudson cryptotephra deposit confounds interpretations of SWW behaviour from all intensity proxies in the sequence except for La/Yb_N, which indicates relatively weak local SWW intensity compared to the mid Holocene. Records from central Chile and the Falklands align with this interpretation, showing a weakening of SWW intensity (Fig. 6b and c, 14) (Lamy et al., 2001; Moreno et al., 2010; Thomas et al., 2018), while records from the core of the SWW in the southwest Pacific see sustained intensity (Fig. 6c,e, 14c,e) (Saunders et al., 2018; Turney et al., 2017). The divergence between these reconstructions indicates the possible onset of asymmetric behaviour in the SWW, either due to a localised latitudinal shift or contraction of the SWW belt from the southeast Pacific to the southwest Atlantic (Fig. 7). Although this is a significant change in SWW behaviour, Patagonia remains the primary distal dust contributor to the Falklands.

The onset of asymmetrical variations in the SWW after 5000 cal yr BP has been recorded across a wide range of proxies and

longitudinal positions (Fletcher and Moreno, 2012), with the most likely cause being a breakdown in the relationship between the SWW and precession-modulated insolation changes. This breakdown has been attributed to the increasing influence of inter-decadal climate modes over the Holocene, such as the El Niño Southern Oscillation, whose onset has been dated to ca. 5000 cal yr BP in the western Pacific and ca. 6000 cal yr BP in the eastern Pacific (Fletcher and Moreno, 2012; Moy et al., 2002; Shulmeister and Lees, 2016; Wanner et al., 2008).

While weakening of the SWW has been reported from central Chile after ca. 3000 cal yr BP (Lamy et al., 2001; Moreno et al., 2021, 2010), the Pond Point record shows extremely strong SWW intensity from 3000 to 1700 cal yr BP. This is demonstrated by the highest dust flux and grain size values on the record outside the influence of tephra deposits, along with strong REE flux and La/Yb_N values (Fig. 3). Consistent with our results, other reconstructions from the southwest Atlantic all see sustained or increased SWW intensity during this period (Fig. 6c and d) (Groff et al., 2020; Moreno et al., 2010; Strother et al., 2015; Thomas et al., 2018). The long term increase of $ssNa^+$ over the mid-to late-Holocene (Fig. 6g) (Mayewski et al., 2013) also implies a deeper (lower pressure) and more intense ASL during this period, with increasing control over southwest Atlantic climate. Therefore, we propose that the increased SWW intensity in these records is due to an eastwards projection of the ASL into the South Atlantic from 3000 to 1700 cal yr BP (Fig. 7) (Thomas et al., 2018), which would increase the ASL's influence over southern South America, the Falklands and South Georgia Island. Although a projection of the ASL is a possible explanation for the divergence in South Atlantic records, more well-dated, multi-proxy reconstructions from the South Atlantic and southern regions of the SWW are needed to confirm its existence and accurately define its boundaries. It is also uncertain to what extent a projection of the ASL would explain the poor agreement between continental South American SWW reconstructions compared to other proposed reasons for disagreement, such as indirect proxies, poorly resolved chronologies and confounding continental influences.

4.6. Linkages to atmospheric CO_2

The cause of mid-to late-Holocene increases in atmospheric CO_2 concentrations (Fig. 6h) (Monnin et al., 2004), not seen in previous interglacial periods, has multiple proposed mechanisms (e.g. anthropogenic land use changes, peat accumulation and the soft tissue carbon pump) (Brovkin et al., 2016). While this study cannot provide insights into the initial increase in CO_2 around ca. 7000 cal yr BP, this rise may be linked to an intensification of the SWW, perhaps triggered by a latitudinal shift of the wind belt or changes to regional sea ice and oceanic temperature gradients (Moreno et al., 2010; Sime et al., 2013).

The mid-Holocene intensification of the SWW described in this study is consistent with prior research demonstrating their role in the ventilation of carbon-rich deep water in the Southern Ocean during this period (Saunders et al., 2018; Toggweiler et al., 2006). This relationship between increasing SWW intensity and CO_2 in the mid-to late-Holocene provides further support for future links between the projected intensification of the SWW and atmospheric CO_2. Given the similarities of our record in the early Holocene with Monteath et al. (2022), which suggests that warmer atmospheric temperatures are associated with a southern movement of the SWW, we propose that periods of higher (lower) SWW intensity in our record are associated with a southwards (northwards) migration of the SWW belt. With this proposed relationship, we interpret that a likely result of a continued poleward migration and intensification of the SWW would be an increase in the upwelling of carbon-rich deep water to the surface of the southern ocean, weakening the Southern Ocean carbon sink (Le Quéré et al., 2007; Toggweiler et al., 2006), and further amplifying the impacts of anthropogenic climate change.

5. Conclusion

The Southern Hemisphere westerly winds are an important component of global climate. However, there is poor agreement on their behaviour on centennial to millennial timescales. This study utilises a multi-proxy approach to create a high-resolution, precisely dated Holocene reconstruction of local SWW intensity from a

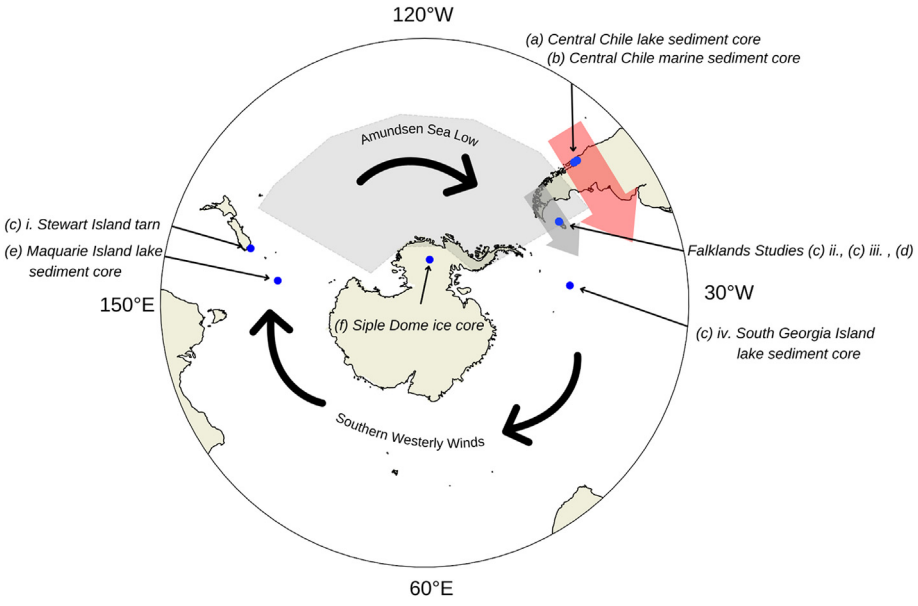

Fig. 7. Location of SWW and atmospheric reconstructions in Fig. 6. Black arrows mark the modern core of the SWW. Red arrow indicates the proposed asymmetric northwards migration or latitudinal contraction of the SWW over the southeast Pacific, southern South America and southwest Atlantic. Grey shaded area marks the range of the modern ASL (Fogt et al., 2012; Thomas et al., 2018). Grey arrow illustrates the proposed projection of the ASL.

Falkland Islands peat core using dust characteristics. These results are compared with other SWW reconstructions from the wider Southern Hemisphere to interpret regional climate dynamics.

We find an increase in SWW intensity over the Falklands in the mid-Holocene, in agreement with other records, which is likely linked to a latitudinal migration or contraction of the wind belt. Importantly, we present evidence that suggests the development of asymmetrical SWW behaviour over southern South America in the late Holocene and propose an associated projection of the Amundsen Sea Low into the South Atlantic. Our results provide an important new reconstruction of SWW behaviour, placing modern changes in a long-term context, and providing new insights into the mechanisms of regional climate dynamics with implications for future global climate.

Author contributions

Jamie Tamhane: Conceptualization, Methodology, Writing - Original Draft, Formal analysis, Investigation, Software. Zoë A. Thomas: Conceptualization, Methodology, Writing - Review & Editing, Supervision, Funding acquisition. Haidee Cadd: Conceptualization, Methodology, Writing - Review & Editing, Supervision. Matthew R.P. Harris: Software, Resources. Chris Turney: Conceptualization, Writing - Review & Editing. Christopher E. Marjo: Methodology. Huixin Wang: Methodology, Investigation. Rabeya Akter: Methodology, Investigation. Panayiotis Panaretos: Investigation. Amalia Hamlin: Investigation. Patricia Gadd: Investigation. Stefanie Carter: Investigation. Paul Brickle: Investigation.

Declaration of competing interest

The authors declare that they have no known competing financial interests or personal relationships that could have appeared to influence the work reported in this paper.

Data availability

All data is attached in the Supplementary Data (Appendix A) with the exception of HYSPLIT trajectories, which will be avaliable on request.

Acknowledgements

We acknowledge Dr Bill Hiscock and Juee Vohra of UNSW MWAC for their work with radiocarbon dating. We would also like to acknowledge the families of Weddell Island, specifically Lewis Clifton, Stephen Clifton, Robert Short and Jo Turner, for facilitating and assisting with field work in the Falkland Islands. This work was supported by an ARC DECRA Fellowship (DE200100907) awarded to Dr Z. Thomas.

Appendix A. Supplementary data

Supplementary data to this article can be found online at https://doi.org/10.1016/j.quascirev.2023.108007.

References

Aldiss, D.T., Edwards, E.J., 1999. The Geology of the Falkand Islands, vol. 226.
Álvarez-Barra, V., Giesecke, T., Fontana, S.L., 2020. Late-Holocene vegetation dynamics and disturbance regimes in north Patagonia Argentina (40°S). Holocene 30, 1115–1128. https://doi.org/10.1177/0959683620913920.
Begum, Z., Balaram, V., Ahmad, S.M., Satyanarayanan, M., Rao, T.G., 2007. Determination of trace and rare earth elements in marine sediment reference materials by ICP-MS: comparison of open and closed acid digestion methods. At. Spectrosc. 28, 41–50.
Bory, A., Wolff, E., Mulvaney, R., Jagoutz, E., Wegner, A., Ruth, U., Elderfield, H., 2010. Multiple sources supply eolian mineral dust to the Atlantic sector of coastal Antarctica: evidence from recent snow layers at the top of Berkner Island ice sheet. Earth Planet Sci. Lett. 291, 138–148. https://doi.org/10.1016/J.EPSL.2010.01.006.
Bozau, E., Lojen, S., Zupančič, N., 2021. The peat bog at Zinnwald-Georgenfeld revisited after 25 years: geochemical investigation of water, Sphagnum moss and peat cores. Geochemistry 125823. https://doi.org/10.1016/J.CHEMER.2021.125823.
Bronk Ramsey, C., 2017. Methods for summarizing radiocarbon datasets. Radiocarbon 59, 1809–1833. https://doi.org/10.1017/RDC.2017.108.
Bronk Ramsey, C., 2009. Dealing with outliers and offsets in radiocarbon dating. Radiocarbon 51, 1023–1045. https://doi.org/10.1017/S0033822200034093.
Bronk Ramsey, C., 2008. Deposition models for chronological records. Quat. Sci. Rev. 27, 42–60. https://doi.org/10.1016/J.QUASCIREV.2007.01.019.
Bronk Ramsey, C., Lee, S., 2013. Recent and planned developments of the program OxCal. Radiocarbon 55, 720–730. https://doi.org/10.1017/S0033822200057878.
Brovkin, V., Brücher, T., Kleinen, T., Zaehle, S., Joos, F., Roth, R., Spahni, R., Schmitt, J., Fischer, H., Leuenberger, M., Stone, E.J., Ridgwell, A., Chappellaz, J., Kehrwald, N., Barbante, C., Blunier, T., Dahl Jensen, D., 2016. Comparative carbon cycle dynamics of the present and last interglacial. Quat. Sci. Rev. 137, 15–32. https://doi.org/10.1016/J.QUASCIREV.2016.01.028.
Browne, I.M., Moy, C.M., Riesselman, C.R., Neil, H.L., Curtin, L.G., Gorman, A.R., Wilson, G.S., 2017. Late Holocene intensification of the westerly winds at the subantarctic Auckland Islands (51° S), New Zealand. Clim. Past 13, 1301–1322. https://doi.org/10.5194/cp-13-1301-2017.
Chagué-Goff, C., Chan, J.C.H., Goff, J., Gadd, P., 2016. Late Holocene record of environmental changes, cyclones and tsunamis in a coastal lake, Mangaia, Cook Islands. Isl. Arc 25, 333–349. https://doi.org/10.1111/IAR.12153.
Chawchai, S., Kylander, M.E., Chabangborn, A., Löwemark, L., Wohlfarth, B., 2016. Testing commonly used X-ray fluorescence core scanning-based proxies for organic-rich lake sediments and peat. Boreas 45, 180–189. https://doi.org/10.1111/BOR.12145.
Clem, K.R., Renwick, J.A., Mcgregor, J., 2017. Large-scale forcing of the Amundsen Sea low and its influence on sea ice and west antarctic temperature. J. Clim. 30, 8405–8424. https://doi.org/10.1175/JCLI-D-16-0891.1.
Croudace, I.W., Rindby, A., Rothwell, R.G., 2006. ITRAX: description and evaluation of a new multi-function X-ray core scanner. Geol. Soc. Spec. Publ. 267, 51–63. https://doi.org/10.1144/GSL.SP.2006.267.01.04.
Cuven, S., Francus, P., Lamoureux, S.F., 2010. Estimation of grain size variability with micro X-ray fluorescence in laminated lacustrine sediments, Cape Bounty, Canadian High Arctic. J. Paleolimnol. 44, 803–817. https://doi.org/10.1007/s10933-010-9453-1.
De Porras, M.E., Mancini, M.V., Prieto, A.R., 2008. Vegetation changes and human occupation in the Patagonian steppe, Argentina, during the late Holocene. Veg. Hist. Archaeobotany 18, 235–244. https://doi.org/10.1007/s00334-008-0200-8.
De Vleeschouwer, F., Vanneste, H., Mauquoy, D., Piotrowska, N., Torrejón, F., Roland, T., Stein, A., Le Roux, G., 2014. Emissions from pre-Hispanic metallurgy in the South American atmosphere. PLoS One 9. https://doi.org/10.1371/journal.pone.0111315.
Dee, D.P., Uppala, S.M., Simmons, A.J., Berrisford, P., Poli, P., Kobayashi, S., Andrae, U., Balmaseda, M.A., Balsamo, G., Bauer, P., Bechtold, P., Beljaars, A.C.M., van de Berg, L., Bidlot, J., Bormann, N., Delsol, C., Dragani, R., Fuentes, M., Geer, A.J., Haimberger, L., Healy, S.B., Hersbach, H., Hólm, E.V., Isaksen, L., Kållberg, P., Köhler, M., Matricardi, M., McNally, A.P., Monge-Sanz, B.M., Morcrette, J.-J., Park, B.-K., Peubey, C., de Rosnay, P., Tavolato, C., Thépaut, J.-N., Vitart, F., 2011. The ERA-Interim reanalysis: configuration and performance of the data assimilation system. Q. J. R. Meteorol. Soc. 137, 553–597. https://doi.org/10.1002/qj.828.
Draxler, R.R., Hess, G.D., 2015. NOAA Technical Memorandum ERL ARL-224 DESCRIPTION of the HYSPLIT_4 MODELING SYSTEM.
Dugmore, A., 2008. Icelandic volcanic ash in Scotland. https://doi.org/10.1080/14702548908554430 105, 168–172. https://doi.org/10.1080/14702548908554430.
Echeverría, M.R., Bamonte, F.P., Marcos, M.A., Sottile, G.D., Mancini, M.V., 2022. Past vegetation reconstruction maps and paleoclimatic variability inferred by pollen records in southern Patagonia Argentina since the Late Glacial-Holocene transition. J. South Am. Earth Sci. 116, 103834. https://doi.org/10.1016/j.jsames.2022.103834.
Etourneau, J., Collins, L.G., Willmott, V., Kim, J.H., Barbara, L., Leventer, A., Schouten, S., Sinninghe Damsté, J.S., Bianchini, A., Klein, V., Crosta, X., Massé, G., 2013. Holocene climate variations in the western Antarctic Peninsula: evidence for sea ice extent predominantly controlled by changes in insolation and ENSO variability. Clim. Past 9, 1431–1446. https://doi.org/10.5194/cp-9-1431-2013.
Evans, C., Artz, R., Moxley, J., Smyth, M.-A., Taylor, E., Archer, N., Burden, A., Williamson, J., Donnelly, D., Thomson, A., Buys, G., Malcolm, H., Wilson, D., Renou-Wilson, F., Potts, J., Chris Evans, P., 2017. Implementation of an Emissions Inventory for UK Peatlands A Report to the Department for Business, Energy & Industrial Strategy Title Implementation of an Emissions Inventory for UK Peatlands.
Fagel, N., Boës, A.X., Loutre, A.M.F., 2008. Climate oscillations evidenced by spectral analysis of Southern Chilean lacustrine sediments: the assessment of ENSO over the last 600 years. https://doi.org/10.1007/s10933-007-9116-z.
Fletcher, M.S., Moreno, P.I., 2012. Have the Southern Westerlies changed in a zonally

symmetric manner over the last 14,000 years? A hemisphere-wide take on a controversial problem. Quat. Int. 253, 32–46. https://doi.org/10.1016/j.quaint.2011.04.042.
Fogt, R.L., Marshall, G.J., 2020. The southern annular mode: variability, trends, and climate impacts across the southern hemisphere. Wiley Interdiscip. Rev. Clim. Chang. 11, 1–24. https://doi.org/10.1002/wcc.652.
Fogt, R.L., Wovrosh, A.J., Langen, R.A., Simmonds, I., 2012. The characteristic variability and connection to the underlying synoptic activity of the Amundsen-Bellingshausen Seas Low. J. Geophys. Res. Atmos. 117. https://doi.org/10.1029/2011JD017337.
Frölicher, T.L., Sarmiento, J.L., Paynter, D.J., Dunne, J.P., Krasting, J.P., Winton, M., 2015. Dominance of the Southern Ocean in anthropogenic carbon and heat uptake in CMIP5 models. J. Clim. 28, 862–886. https://doi.org/10.1175/JCLI-D-14-00117.1.
Gaiero, D.M., Depetris, P.J., Probst, J.L., Bidart, S.M., Leleyter, L., 2004. The signature of river- and wind-borne materials exported from Patagonia to the southern latitudes: a view from REEs and implications for paleoclimatic interpretations. Earth Planet Sci. Lett. 219, 357–376. https://doi.org/10.1016/S0012-821X(03)00686-1.
Garreaud, R., Lopez, P., Minvielle, M., Rojas, M., 2013. Large-scale control on the Patagonian climate. J. Clim. 26, 215–230. https://doi.org/10.1175/JCLI-D-12-00001.1.
Gassó, S., Torres, O., 2019. Temporal characterization of dust activity in the central patagonia desert (years 1964–2017). J. Geophys. Res. Atmos. 124, 3417–3434. https://doi.org/10.1029/2018JD030209.
Gili, S., Gaiero, D.M., Goldstein, S.L., Chemale, F., Jweda, J., Kaplan, M.R., Becchio, R.A., Koester, E., 2017. Glacial/interglacial changes of Southern Hemisphere wind circulation from the geochemistry of South American dust. Earth Planet Sci. Lett. 469, 98–109. https://doi.org/10.1016/j.epsl.2017.04.007.
Gray, W.R., DeLavergne, C., J Wills, R.C., Menviel, L., Spence, P., Kageyama, M., Michel, E., 2021. In Press. Poleward Shift in the Southern Hemisphere Westerly Winds 1 Synchronous with the Deglacial Rise in CO2 2 3. EarthArXiv.
Groff, D.V., Hamley, K.M., Lessard, T.J.R., Greenawalt, K.E., Yasuhara, M., Brickle, P., Gill, J.L., 2020. Seabird establishment during regional cooling drove a terrestrial ecosystem shift 5000 years ago. Sci. Adv. 6. https://doi.org/10.1126/SCIADV.ABB2788.
Haug, G.H., Hughen, K.A., Sigman, D.M., Peterson, L.C., Röhl, U., 2001. Southward migration of the intertropical convergence zone through the holocene. Science 84 293, 1304–1308. https://doi.org/10.1126/science.1059725.
Heiri, O., Lotter, A.F., Lemcke, G., 2001. Loss on ignition as a method for estimating organic and carbonate content in sediments: reproducibility and comparability of results. J. Paleolimnol. 25, 101–110.
Hill, K.J., Santoso, A., England, M.H., 2009. Interannual Tasmanian rainfall variability associated with large-scale climate modes. J. Clim. 22, 4383–4397. https://doi.org/10.1175/2009JCLI2769.1.
Hogg, A.G., Heaton, T.J., Hua, Q., Palmer, J.G., Turney, C.S.M., Southon, J., Bayliss, A., Blackwell, P.G., Boswijk, G., Bronk Ramsey, C., Pearson, C., Petchey, F., Reimer, P., Reimer, R., Wacker, L., 2020. SHCal20 southern hemisphere calibration, 0-55,000 Years cal BP. Radiocarbon 62, 759–778. https://doi.org/10.1017/RDC.2020.59.
Hooper, J., Marx, S.K., May, J.H., Lupo, L.C., Kulemeyer, J.J., Pereira, E. de los Á., Seki, O., Heijnis, H., Child, D., Gadd, P., Zawadzki, A., 2020. Dust deposition tracks late-Holocene shifts in monsoon activity and the increasing role of human disturbance in the Puna-Altiplano, northwest Argentina. Holocene 30, 519–536. https://doi.org/10.1177/0959683619895814.
Hosking, J.S., Orr, A., Marshall, G.J., Turner, J., Phillips, T., 2013. The influence of the amundsen-bellingshausen seas low on the climate of West Antarctica and its representation in coupled climate model simulations. J. Clim. 26, 6633–6648. https://doi.org/10.1175/JCLI-D-12-00813.1.
Hua, Q., Barbetti, M., Rakowski, A.Z., 2013. Atmospheric radiocarbon for the period 1950–2010. Radiocarbon 55, 2059–2072. https://doi.org/10.2458/azu_js_rc.v55i2.16177.
Huber, U.M., Markgraf, V., 2003. European impact on fire regimes and vegetation dynamics at the steppe-forest ecotone of southern Patagonia. Holocene 13, 567–579. https://doi.org/10.1191/0959683603hl647rp.
Jara, I.A., Moreno, P.I., Alloway, B.V., Newnham, R.M., 2019. A 15,400-year long record of vegetation, fire-regime, and climate changes from the northern Patagonian Andes. Quat. Sci. Rev. 226, 106005. https://doi.org/10.1016/j.quascirev.2019.106005.
Jenny, B., Wilhelm, D., Valero-Garcés, B.L., 2003. The Southern Westerlies in Central Chile: holocene precipitation estimates based on a water balance model for Laguna Aculeo (33°50′S). Clim. Dynam. 20, 269–280. https://doi.org/10.1007/s00382-002-0267-3.
Kalnay, E., Kanamitsu, M., Kistler, R., Collins, W., Deaven, D., Gandin, L., Iredell, M., Saha, S., White, G., Woollen, J., Zhu, Y., Chelliah, M., Ebisuzaki, W., Higgins, W., Janowiak, J., Mo, K.C., Ropelewski, C., Wang, J., Leetmaa, A., Reynolds, R., Jenne, R., Joseph, D., 1996. The NCEP/NCAR 40-year reanalysis project. Bull. Am. Meteorol. Soc. 77, 437–471. https://doi.org/10.1175/1520-0477(1996)077<0437:TNYRP>2.0.CO;2.
Kaplan, M.R., Schaefer, J.M., Strelin, J.A., Denton, G.H., Anderson, R.F., Vandergoes, M.J., Finkel, R.C., Schwartz, R., Travis, S.G., Garcia, J.L., Martini, M.A., Nielsen, S.H.H., 2016. Patagonian and southern South Atlantic view of holocene climate. Quat. Sci. Rev. 141, 112–125. https://doi.org/10.1016/j.quascirev.2016.03.014.
Kaplan, M.R., Strelin, J.A., Schaefer, J.M., Peltier, C., Martini, M.A., Flores, E., Winckler, G., Schwartz, R., 2020. Holocene glacier behavior around the northern Antarctic Peninsula and possible causes. Earth Planet Sci. Lett. 534. https://doi.org/10.1016/j.epsl.2020.116077.
Kilian, R., Lamy, F., 2012. A review of Glacial and Holocene paleoclimate records from southernmost Patagonia (49-55°S). Quat. Sci. Rev. 53, 1–23. https://doi.org/10.1016/j.quascirev.2012.07.017.
Klaes, B., Wörner, G., Kremer, K., Simon, K., Kronz, A., Scholz, D., Mueller, C.W., Höschen, C., Struck, J., Arz, H.W., Thiele-Bruhn, S., Schimpf, D., Kilian, R., 2022. High-resolution stalagmite stratigraphy supports the Late Holocene tephrochronology of southernmost Patagonia. Commun. Earth Environ. 3, 1–15. https://doi.org/10.1038/s43247-022-00358-0.
Kohfeld, K.E., Graham, R.M., de Boer, A.M., Sime, L.C., Wolff, E.W., Le Quéré, C., Bopp, L., 2013. Southern hemisphere westerly wind changes during the last glacial maximum: paleo-data synthesis. Quat. Sci. Rev. 68, 76–95. https://doi.org/10.1016/j.quascirev.2013.01.017.
Lamy, F., Hebbeln, D., Röhl, U., Wefer, G., 2001. Holocene rainfall variability in Southern Chile: a marine record of latitudinal shifts of the Southern Westerlies. Earth Planet Sci. Lett. 185, 369–382. https://doi.org/10.1016/S0012-821X(00)00381-2.
Landschützer, P., Gruber, N., Haumann, F.A., Rödenbeck, C., Bakker, D.C.E., Heuven, S. Van, Hoppema, M., Metzl, N., Sweeney, C., Takahashi, T., 2015. Ocean carbon sink. Science (80-) 349, 1221–1224.
Le Quéré, C., Rödenbeck, C., Buitenhuis, E.T., Conway, T.J., Langenfelds, R., Gomez, A., Labuschagne, C., Ramonet, M., Nakazawa, T., Metzl, N., Gillett, N., Heimann, M., 2007. Saturation of the southern ocean CO2 sink due to recent climate change. Science (80-) 316, 1735–1738. https://doi.org/10.1126/science.1136188.
Lewis, R.J., Tibby, J., Arnold, L.J., Barr, C., Marshall, J., McGregor, G., Gadd, P., Yokoyama, Y., 2020. Insights into subtropical Australian aridity from Welsby Lagoon, north Stradbroke Island, over the past 80,000 years. Quat. Sci. Rev. 234, 106262. https://doi.org/10.1016/j.quascirev.2020.106262.
Li, C., Sonke, J.E., Le Roux, G., Van der Putten, N., Piotrowska, N., Jeandel, C., Mattielli, N., Benoit, M., Wiggs, G.F.S., De Vleeschouwer, F., 2020. Holocene dynamics of the southern westerly winds over the Indian Ocean inferred from a peat dust deposition record. Quat. Sci. Rev. 231, 1–13. https://doi.org/10.1016/j.quascirev.2020.106169.
Lister, D.H., Jones, P.D., 2014. Long-term temperature and precipitation records from the Falkland Islands. Int. J. Climatol. 35, 1224–1231. https://doi.org/10.1002/joc.4049.
Longman, J., Veres, D., Ersek, V., Salzmann, U., Hubay, K., Bormann, M., Wennrich, V., Schäbitz, F., 2017. Periodic input of dust over the Eastern Carpathians during the Holocene linked with Saharan desertification and human impact. Clim. Past 13, 897–917. https://doi.org/10.5194/cp-13-897-2017.
Longman, J., Veres, D., Wennrich, V., 2019. Utilisation of XRF core scanning on peat and other highly organic sediments. Quat. Int. 514, 85–96. https://doi.org/10.1016/j.quaint.2018.10.015.
Mancini, M.V., 2009. Holocene vegetation and climate changes from a peat pollen record of the forest - steppe ecotone, Southwest of Patagonia (Argentina). Quat. Sci. Rev. 28, 1490–1497. https://doi.org/10.1016/j.quascirev.2009.01.017.
Markgraf, V., Baumgartner, T.R., Bradbury, J.P., Diaz, H.F., Dunbar, R.B., Luckman, B.H., Seltzer, G.O., Swetnam, T.W., Villalba, R., 2000. Paleoclimate reconstruction along the Pole-Equator-Pole transect of the americas (PEP 1). Quat. Sci. Rev. 19, 125-140.
Marshall, G.J., 2021. An Observation-Based Southern Hemisphere Annular Mode Index.
Marshall, G.J., 2003. Trends in the southern annular mode from observations and reanalyses. J. Clim. 16, 4134–4143. https://doi.org/10.1175/1520-0442(2003)016<4134:TITSAM>2.0.CO;2.
Marx, S.K., McGowan, H.A., Kamber, B.S., 2009. Long-range dust transport from eastern Australia: a proxy for Holocene aridity and ENSO-type climate variability. Earth Planet Sci. Lett. 282, 167–177. https://doi.org/10.1016/j.epsl.2009.03.013.
Marx, S.K.S.K., Kamber, B.S.B.S., McGowan, H.A.H.A., Petherick, L.M.L.M., McTainsh, G.H.G.H., Stromsoe, N., Hooper, J.N.J.N., May, J.-H.J.H., 2018. Palaeodust records: a window to understanding past environments. Global Planet. Change 165, 13–43. https://doi.org/10.1016/j.gloplacha.2018.03.001.
Mayewski, P.A., Maasch, K.A., Dixon, D., Sneed, S.B., Oglesby, R., Korotkikh, E., Potocki, M., Grigholm, B., Kreutz, K., Kurbatov, A.V., Spaulding, N., Stager, J.C., Taylor, K.C., Steig, E.J., White, J., Bertler, N.A.N., Goodwin, I., Simões, J.C., Jaña, R., Kraus, S., Fastook, J., 2013. West Antarctica's sensitivity to natural and human-forced climate change over the Holocene. J. Quat. Sci. 28, 40–48. https://doi.org/10.1002/JQS.2593.
Mercer, J., Ager, T., 1983. Glacial and floral changes in southern Argentina since 14,000 years ago. Natl. Geogr. Soc. Res. Reports 15, 457–477.
Met Office, 2007. Met Office Mount Pleasant, Falkland Islands, High Resolution Radiosonde Data. NCAS British Atmospheric Data Centre.
Monnin, E., Steig, E.J., Siegenthaler, U., Kawamura, K., Schwander, J., Stauffer, B., Stocker, T.F., Morse, D.L., Barnola, J.M., Bellier, B., Raynaud, D., Fischer, H., 2004. Evidence for substantial accumulation rate variability in Antarctica during the Holocene, through synchronization of CO2 in the Taylor Dome, Dome C and DML ice cores. Earth Planet Sci. Lett. 224, 45–54. https://doi.org/10.1016/J.EPSL.2004.05.007.
Monteath, A., Hughes, P., Cooper, M., Groff, D., Scaife, R., Hodgson, D., 2022. Late glacial–holocene record of southern hemisphere westerly wind dynamics from the Falkland Islands, South Atlantic ocean. Geology 50, 880–885. https://doi.org/10.1130/G49805.1.

Monteath, A.J., Hughes, P.D.M., Wastegård, S., 2019. Evidence for distal transport of reworked Andean tephra: extending the cryptotephra framework from the Austral volcanic zone. Quat. Geochronol. 51, 64–71. https://doi.org/10.1016/J.QUAGEO.2019.01.003.

Moreno, P.I., 2004. Millennial-scale climate variability in northwest Patagonia over the last 15 000 yr. J. Quat. Sci. 19, 35–47. https://doi.org/10.1002/jqs.813.

Moreno, P.I., Francois, J.P., Moy, C.M., Villa-Martínez, R., 2010. Covariability of the southern westerlies and atmospheric CO2 during the holocene. Geology 38, 727–730. https://doi.org/10.1130/G30962.1.

Moreno, P.I., Henríquez, W.I., Pesce, O.H., Henríquez, C.A., Fletcher, M.S., Garreaud, R.D., Villa-Martínez, R.P., 2021. An early Holocene westerly minimum in the southern mid-latitudes. Quat. Sci. Rev. 251, 106730. https://doi.org/10.1016/j.quascirev.2020.106730.

Moy, C.M., Seltzer, G.O., Rodbell, D.T., Anderson, D.M., 2002. Variability of El niño/southern oscillation activity at millennial timescales during the holocene epoch. Nat 2002, 162–165. https://doi.org/10.1038/nature01194, 4206912 420.

Munro, D.R., Lovenduski, N.S., Takahashi, T., Stephens, B.B., Newberger, T., Sweeney, C., 2015. Recent evidence for a strengthening CO $_2$ sink in the Southern Ocean from carbonate system measurements in the Drake Passage (2002–2015). Geophys. Res. Lett. 42, 7623–7630. https://doi.org/10.1002/2015GL065194.

Novak, M., Zemanova, L., Voldrichova, P., Stepanova, M., Adamova, M., Pacherova, P., Komarek, A., Krachler, M., Prechova, E., 2011. Experimental evidence for mobility/immobility of metals in peat. Environ. Sci. Technol. 45, 7180–7187. https://doi.org/10.1021/ES201086V.

Oksanen, J., Blanchet, F.G., Friendly, M., Kindt, R., Legendre, P., Mcglinn, D., Minchin, P.R., O'hara, R.B., Simpson, G.L., Solymos, P., Henry, M., Stevens, H., Szoecs, E., Maintainer, H.W., 2020. Package "Vegan" Title Community Ecology Package Version 2, pp. 5–7.

Panaretos, P., Albert, P.G., Thomas, A., Turney, C.S., Stern, C.R., Jones, G., Williams, A.N., Smith, V.C., Hogg, A.G., Manning, C.J., 2021. Distal ash fall from the mid-Holocene eruption of Mount Hudson (H2) discovered in the Falkland Islands: new possibilities for Southern Hemisphere archive synchronisation. https://doi.org/10.1016/j.quascirev.2021.107074.

Pendall, E., Markgraf, V., White, J.W.C., Dreier, M., 2001. Multiproxy record of late pleistocene-holocene climate and vegetation changes from a peat bog in patagonia. Quat. Res. 55, 168–178. https://doi.org/10.1006/qres.2000.2206.

Perren, B.B., Hodgson, D.A., Roberts, S.J., Sime, L., Van Nieuwenhuyze, W., Verleyen, E., Vyverman, W., 2020. Southward migration of the Southern Hemisphere westerly winds corresponds with warming climate over centennial timescales. Commun. Earth Environ. 2020 11 (1), 1–8. https://doi.org/10.1038/s43247-020-00059-6.

Pilcher, J.R., Hall, V.A., 1992. Towards a tephrochronology for the Holocene of the north of Ireland. Holocene 2, 255–259. https://doi.org/10.1177/095968369200200307.

Raut, B.A., Jakob, C., Reeder, M.J., 2014. Rainfall changes over Southwestern Australia and their relationship to the southern annular mode and ENSO. J. Clim. 27, 5801–5814. https://doi.org/10.1175/JCLI-D-13-00773.1.

Risbey, J.S., Pook, M.J., McIntosh, P.C., Wheeler, M.C., Hendon, H.H., 2009. On the remote drivers of rainfall variability in Australia. Mon. Weather Rev. 137, 3233–3253. https://doi.org/10.1175/2009MWR2861.1.

Rothwell, J.J., Taylor, K.G., Chenery, S.R.N., Cundy, A.B., Evans, M.G., Allott, T.E.H., 2010. Storage and behavior of As, Sb, Pb, and Cu in ombrotrophic peat bogs under contrasting water table conditions. Environ. Sci. Technol. 44, 8497–8502. https://doi.org/10.1021/es101150w.

Saunders, K.M., Roberts, S.J., Perren, B., Butz, C., Sime, L., Davies, S., Van Nieuwenhuyze, W., Grosjean, M., Hodgson, D.A., 2018. Holocene dynamics of the Southern Hemisphere westerly winds and possible links to CO2 outgassing. Nat. Geosci. 11, 650–655. https://doi.org/10.1038/s41561-018-0186-5.

Shevenell, A.E., Ingalls, A.E., Domack, E.W., Kelly, C., 2011. Holocene Southern Ocean surface temperature variability west of the antarctic Peninsula. Nature 470, 250–254. https://doi.org/10.1038/nature09751.

Shindell, D.T., Schmidt, G.A., 2004. Southern Hemisphere climate response to ozone changes and greenhouse gas increases. Geophys. Res. Lett. 31, L18209. https://doi.org/10.1029/2004GL020724.

Shulmeister, J., Lees, B.G., 2016. Pollen evidence from tropical Australia for the onset of an ENSO-dominated climate at c. 4000 BP. https://doi.org/10.1177/095968369500500102 5, 10–18. https://doi.org/10.1177/095968369500500102.

Sime, L.C., Kohfeld, K.E., Le Quéré, C., Wolff, E.W., de Boer, A.M., Graham, R.M., Bopp, L., 2013. Southern hemisphere westerly wind changes during the last glacial maximum: model-data comparison. Quat. Sci. Rev. 64, 104–120. https://doi.org/10.1016/j.quascirev.2012.12.008.

Smith, R.E., Smith, V.C., Fontijn, K., Gebhardt, A.C., Wastegård, S., Zolitschka, B., Ohlendorf, C., Stern, C., Mayr, C., 2019. Refining the late quaternary tephrochronology for southern SouthSouth America using the laguna potrok aike sedimentary record. Quat. Sci. Rev. 218, 137–156. https://doi.org/10.1016/J.QUASCIREV.2019.06.001.

Stern, C.R., 2008. Holocene tephrochronology record of large explosive eruptions in the southernmost Patagonian Andes. Bull. Volcanol. 70, 435–454. https://doi.org/10.1007/s00445-007-0148-z.

Stone, P., 2015. Geology reviewed for the Falkland Islands and their offshore sedimentary basins, South Atlantic Ocean. Earth Environ. Sci. Trans. R. Soc. Edinburgh 106, 115–143. https://doi.org/10.1017/S1755691016000049.

Strother, S.L., Salzmann, U., Roberts, S.J., Hodgson, D.A., Woodward, J., Van Nieuwenhuyze, W., Verleyen, E., Vyverman, W., Moreton, S.G., 2015. Changes in Holocene climate and the intensity of Southern Hemisphere Westerly Winds based on a high-resolution palynological record from sub-Antarctic South Georgia. Holocene 25, 263–279. https://doi.org/10.1177/0959683614557576.

Stuut, J.B.W., Prins, M.A., Schneider, R.R., Weltje, G.J., Fred Jansen, J.H., Postma, G., 2002. A 300-kyr record of aridity and wind strength in southwestern Africa: inferences from grain-size distributions of sediments on Walvis Ridge, SE Atlantic. Mar. Geol. 180, 221–233. https://doi.org/10.1016/S0025-3227(01)00215-8.

Swart, N.C., Fyfe, J.C., 2012. Observed and simulated changes in the Southern Hemisphere surface westerly wind-stress. Geophys. Res. Lett. 39. https://doi.org/10.1029/2012GL052810.

Taylor, S.R., McLennan, S.M., 1995. The geochemical the continental evolution crust. Rev. Mineral. Geochem. 33, 241–265.

Thomas, Z.A., Jones, R.T., Fogwill, C.J., Hatton, J., Williams, A.N., Hogg, A., Mooney, S., Jones, P., Lister, D., Mayewski, P., Turney, C.S.M., 2018. Evidence for increased expression of the Amundsen Sea Low over the South Atlantic during the late holocene. Clim. Past 14, 1727–1738. https://doi.org/10.5194/cp-14-1727-2018.

Thomas, Z.A., Turney, C.S.M., Hogg, A., Williams, A.N., Fogwill, C.J., 2019. Investigating subantarctic 14C ages of different peat components: site and sample selection for developing robust age models in dynamic landscapes. Radiocarbon 61, 1009–1027. https://doi.org/10.1017/RDC.2019.54.

Thompson, D.W.J., Solomon, S., 2002. Interpretation of recent Southern Hemisphere climate change. Science. 296 (5569), 895–899.

Toggweiler, J.R., Russell, J.L., Carson, S.R., 2006. Midlatitude westerlies, atmospheric CO2, and climate change during the ice ages. Paleoceanography 21, 1–15. https://doi.org/10.1029/2005PA001154.

Tonello, M.S., Mancini, M.V., Seppä, H., 2009. Quantitative reconstruction of Holocene precipitation changes in southern Patagonia. Quat. Res. 72, 410–420. https://doi.org/10.1016/j.yqres.2009.06.011.

Turney, C., Becerra-Valdivia, L., Sookdeo, A., Thomas, Z.A., Palmer, J., Haines, H.A., Cadd, H., Wacker, L., Baker, A., Andersen, M.S., Jacobsen, G., Meredith, K., Chinu, K., Bollhalder, S., Marjo, C., 2021. Radiocarbon protocols and first intercomparison results from the chronos 14Carbon-cycle facility, university of New South Wales, sydney, Australia. Radiocarbon 63, 1003–1023. https://doi.org/10.1017/RDC.2021.23.

Turney, C., Fogwill, C., 2021. The implications of the recently recognized mid-20th century shift in the Earth system. Anthropol. Rev. https://doi.org/10.1177/2053019621995526.

Turney, C.S.M., Jones, R.T., Fogwill, C., Hatton, J., Williams, A.N., Hogg, A., Thomas, Z.A., Palmer, J., Mooney, S., Reimer, R.W., 2016. A 250-year periodicity in Southern Hemisphere westerly winds over the last 2600 years. Clim. Past 12, 189–200. https://doi.org/10.5194/cp-12-189-2016.

Turney, C.S.M., Wilmshurst, J.M., Jones, R.T., Wood, J.R., Palmer, J.G., Hogg, A.G., Fenwick, P., Crowley, S.F., Privat, K., Thomas, Z., 2017. Reconstructing atmospheric circulation over southern New Zealand: establishment of modern westerly airflow 5500 years ago and implications for Southern Hemisphere Holocene climate change. Quat. Sci. Rev. 159, 77–87. https://doi.org/10.1016/j.quascirev.2016.12.017.

Upton, J., Shaw, C.J., 2002. An overview of the oceanography and meteorology of the Falkland Islands. Aquat. Conserv. Mar. Freshw. Ecosyst. 12, 15–25. https://doi.org/10.1002/AQC.496.

Vanneste, H., De Vleeschouwer, F., Bertrand, S., Martínez-Cortizas, A., Vanderstraeten, A., Mattielli, N., Coronato, A., Piotrowska, N., Jeandel, C., Roux, G. Le, 2016. Elevated dust deposition in Tierra del Fuego (Chile) resulting from Neoglacial Darwin Cordillera glacier fluctuations. J. Quat. Sci. 31, 713–722. https://doi.org/10.1002/jqs.2896.

Varma, V., Prange, M., Lamy, F., Merkel, U., Schulz, M., 2011. Solar-forced shifts of the southern hemisphere westerlies during the holocene. Clim. Past 7, 339–347. https://doi.org/10.5194/cp-7-339-2011.

Voigt, I., Chiessi, C.M., Prange, M., Mulitza, S., Groeneveld, J., Varma, V., Henrich, R., 2015. Holocene shifts of the southern westerlies across the South Atlantic. Paleoceanography 30, 39–51. https://doi.org/10.1002/2014PA002677.

Wanner, H., Beer, J., Bütikofer, J., Crowley, T.J., Cubasch, U., Flückiger, J., Goosse, H., Grosjean, M., Joos, F., Kaplan, J.O., Küttel, M., Müller, S.A., Prentice, I.C., Solomina, O., Stocker, T.F., Tarasov, P., Wagner, M., Widmann, M., 2008. Mid- to Late Holocene climate change: an overview. Quat. Sci. Rev. 27, 1791–1828. https://doi.org/10.1016/J.QUASCIREV.2008.06.013.

Watt, S.F.L., Pyle, D.M., Mather, T.A., 2013. Evidence of mid- to late-Holocene explosive rhyolitic eruptions from Chaitén Volcano, Chile. Andean Geol. 40, 216–226. https://doi.org/10.5027/andgeoV40n2-a02.

Wilson, P., Clark, R., Birnie, J., Moore, D.M., 2002. Late pleistocene and holocene landscape evolution and environmental change in the lake sulivan area, Falkland Islands, South Atlantic. Quat. Sci. Rev. 21, 1821–1840. https://doi.org/10.1016/S0277-3791(02)00008-2.

Yang, L., Jiang, M., Zou, Y., Qin, L., Chen, Y., 2021. Geographical distribution of iron redox cycling bacterial community in peatlands: distinct assemble mechanism across environmental gradient. Front. Microbiol. 12. https://doi.org/10.3389/fmicb.2021.674411.